Available online at www.sciencedirect.com
SCIENCE DIRECT®
Fusion Engineering and Design 65 (2003) 215–261
Fusion Engineering and Design
www.elsevier.com/locate/fusengdes

Fusion power core engineering for the ARIES-ST power plant

M.S. Tillack [a,*], X.R. Wang [a], J. Pulsifer [a], S. Malang [b], D.K. Sze [c], M. Billone [c], I. Sviatoslavsky [d], ARIES Team

[a] *Fusion Energy Research Program, University of California, 460 EBUII, La Jolla, San Diego, CA 92093-0417, USA*
[b] *Forschungszentrum Karlsruhe, Karlsruhe, Germany*
[c] *Argonne National Laboratory, Argonne, IL, USA*
[d] *University of Wisconsin, Madison, WI, USA*

Abstract

ARIES-ST is a 1000 MWe fusion power plant based on a low aspect ratio 'spherical torus' (ST) plasma. The ARIES-ST power core was designed to accommodate the unique features of an ST power plant, to meet the top-level requirements of an attractive fusion energy source, and to minimize extrapolation from the fusion technology database under development throughout the world. The result is an advanced helium-cooled ferritic steel blanket with flowing PbLi breeder and tungsten plasma-interactive components. Design improvements, such as the use of SiC inserts in the blanket to extend the outlet coolant temperature range were explored and the results are reported here. In the final design point, the power and particle loads found in ARIES-ST are relatively similar to other advanced tokamak power plants (e.g. ARIES-RS [Fusion Eng. Des. 38 (1997) 3; Fusion Eng. Des. 38 (1997) 87]) such that exotic technologies were not required in order to satisfy all of the design criteria. Najmabadi and the ARIES Team [Fusion Eng. Des. (this issue)] provide an overview of ARIES-ST design. In this article, the details of the power core design are presented together with analysis of the thermal–hydraulic, thermomechanical and materials behavior of in-vessel components. Detailed engineering analysis of ARIES-ST TF and PF systems, nuclear analysis, and safety are given in the companion papers [4–7].
© 2002 Elsevier Science B.V. All rights reserved.

Keywords: Spherical torus; ARIES-ST power plant; Advanced tokamak

1. Introduction

The ARIES-ST study is a national US effort to investigate the potential of the spherical tokamak concept as a fusion power plant and as a vehicle for fusion development. Theoretical and experimental studies indicate that the MHD performance of a tokamak plasma is substantially improved with decreasing aspect ratio. While steady-state tokamaks with superconducting toroidal-field (TF) coils optimize at moderately high aspect ratio ($A \sim 4$), at low aspect ratio the plasma β becomes large enough and the required TF becomes small enough that resistive TF coils with manageable Joule losses can be used. This elim-

* Corresponding author. Tel.: +1-858-5347897; fax: +1-858-5347716.
E-mail address: tillack@fusion.ucsd.edu (M.S. Tillack).

0920-3796/03/$ - see front matter © 2002 Elsevier Science B.V. All rights reserved.
PII: S0920-3796(02)00305-8

inates the need for a thick, inboard shield for cryogenic TF coils so that fusion devices with smaller major radius may be possible.

ARIES-ST is a 1000-MWe power plant with an aspect ratio of 1.6, a major radius of 3.2 m, a plasma elongation of 3.4 and triangularity of 0.64. This configuration attains a β of 54% (which is 90% of the maximum theoretical β). While the plasma current is 31 MA, the almost perfect alignment of bootstrap and equilibrium current density profiles results in a current-drive power of only 31 MW. The on-axis TF is 2.1 T and the peak field at the TF coil is 7.6 T, which leads to 288 MW of Joule losses in the normal-conducting TF system.

The ARIES-ST power core consists of the components directly surrounding the burning plasma, and serves several important functions. Energy released by fusion reactions (as well as energy injected for plasma heating and current drive) is extracted at high temperature to produce electricity. In addition, the power core is responsible for producing sufficient tritium to sustain the DT fusion reaction and for shielding the magnets and other in-vessel components. The power core experiences the most severe thermomechanical and radiation environment, and thus its performance limits have the most profound impact on the plant economic, safety and environmental features.

The ARIES-ST power core was designed for compatibility with an optimized ST plasma that evolved through the exploration of a wide range of plasma MHD equilibria [8]. In addition, the design was influenced strongly by the top-level requirements for a desirable fusion energy source [9]. These include a set of economic attributes as well as strict safety and waste criteria intended to result in a licensable plant. Extrapolation from known technologies introduces significant risk, and entails a potentially large R&D program. However, extrapolation is inevitable, given the substantial gap between the existing database and the high level of performance required for an attractive fusion power plant. In ARIES-ST, radically new design concepts were not perceived as necessary. Instead, an approach was taken to extend and improve more conventional design concepts that have enjoyed the attention of fusion R&D programs throughout the world, and to determine whether these technologies are capable of satisfying the design requirements.

Some of the unique features of the ARIES-ST power plant include the following:

1) the use of water coolant in the power core (for the copper centerpost) strongly discourages the use of reactive materials such as lithium and beryllium.
2) High thermal conversion efficiency is needed to offset the effect of high re-circulating power in the normal-conducting TF system.
3) Relatively high power density results from the extraordinarily high plasma β.
4) The absence of space on the inboard side for a breeding blanket places additional constraints on material selection and dimensions.
5) The highly elongated plasma together with an integrated outboard TF shell and vacuum vessel led to a vertical maintenance scheme and toroidally integrated blanket.

The flux surface configuration of ARIES-ST is similar to a 'normal' tokamak with a double null (see Fig. 1), except that the plasma is highly elongated ($\kappa = 3.75$ at the $\times$-point) to increase the maximum stable plasma β ($\sim 55\%$). Due to expectations of low transport power on the inboard side [10], and also due to the lack of space to accommodate a full inboard divertor, inboard transport power flows are distributed along the entire first wall rather than being concentrated in a closed inboard divertor slot. Relatively large core radiation fraction (45%) is achieved using injected impurities, such that the total power into the outboard divertor slot remains modest.

The power flows in the high-temperature components are summarized in Table 1 and the peak and average values of neutron wall loading and surface heat flux are shown in Table 2. Fig. 2 shows the distribution of neutron wall loading for the plasma-facing components [6] and Fig. 3 shows the transport power flows which result in surface heat loads. Although the major radius of ARIES-ST is small, the large height results in a first wall area similar to (or larger than) a 'standard' aspect ratio tokamak. In addition, the plasma volumetric

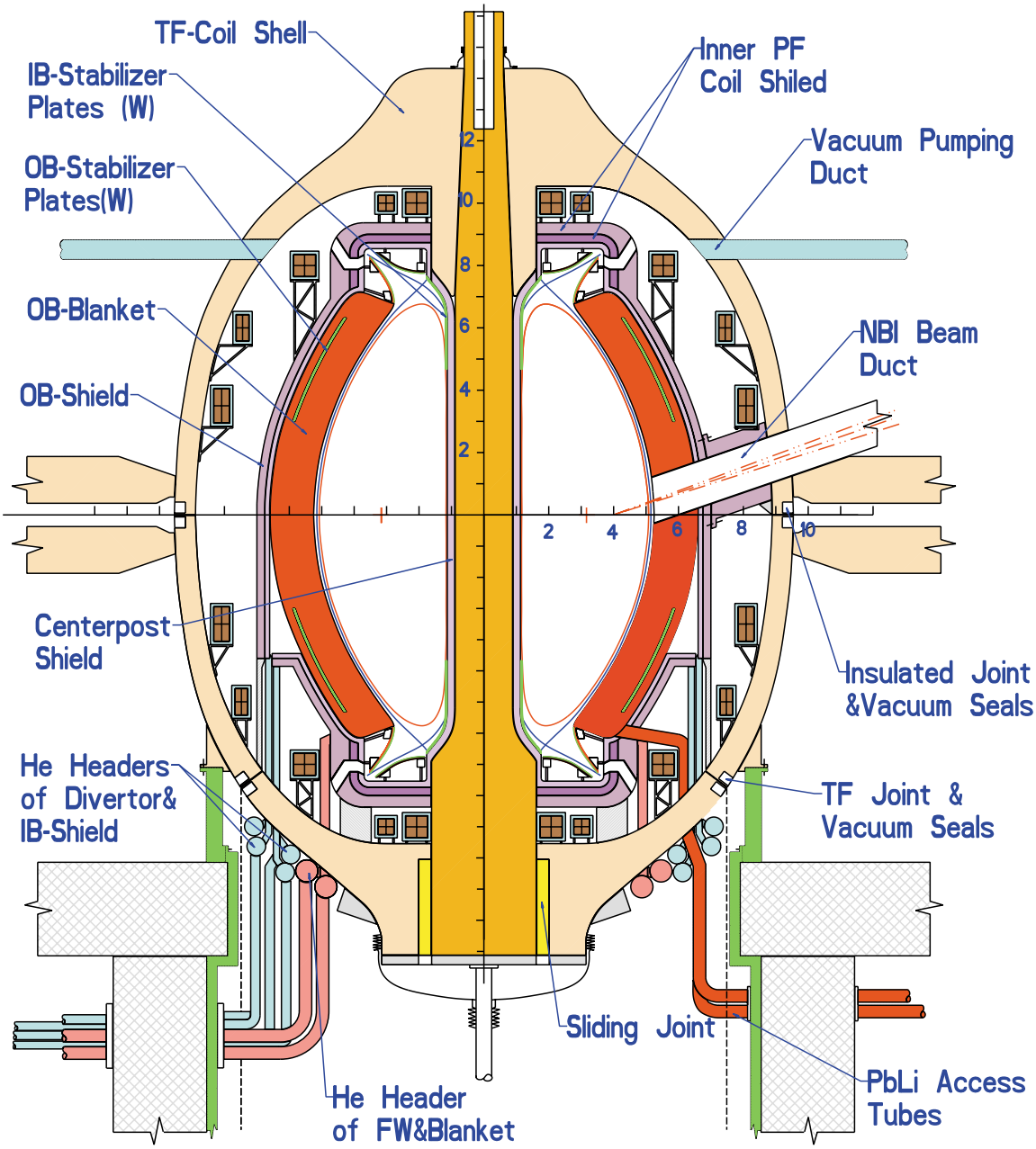

Fig. 1. Elevation view of the ARIES-ST power core.

power density is not unusually high. The low TF strength compensates the high average plasma β, such that the volumetric power density—which is proportional to $\beta^2\beta^4$—is actually smaller than a 'standard' aspect ratio tokamak.

Core transport power is partitioned into radiation and particle flows. Since the outboard first wall is positioned well outside the scrape-off layer, the particle flows are assumed to deposit their energy on the divertor and on the inboard first

Table 1
Summary of power flows in high-temperature regions

	Area (m^2)	Nuclear heating (MW) [c]	Surface heating (MW)	Total power (MW)
Outboard first wall	421	100	195	295
Inboard first wall	67	18	52	70
Inboard stability shells	54	71	73	144
Inboard shield		199	0	199
Divertor	128	201[a]	250	451
Outboard ferritic steel	–	330 [a,b]	–	330
Outboard PbLi	–	1614 [b]	–	1614
Total	–	2533	570	3103

[a] Includes heating in manifolds and high-temperature shield.
[b] Includes 110 MW conducted from PbLi to He.
[c] Includes energy multiplication.

Table 2
Peak and average values of neutron wall load and surface heat flux

	Neutron wall load (MW/m^2)		Surface heat flux (MW/m^2)	
	Average	Peak	Average	Peak
First wall	4.2	6.0	0.46	0.6
Divertor	–	–	2.0	6.0

wall and stability shells. About 20% of this power is assumed to be deposited on the inboard side of the machine; this is considered a conservative estimate for physics reasons [10] and also because handling power on the inboard first wall is a more challenging task than handling it in the divertor. As shown in Fig. 3, this results in 125 MW on the inboard surfaces and 251 MW on the divertor plates.

Fig. 1 shows a cross section of the power core in its normal operating position within the vacuum

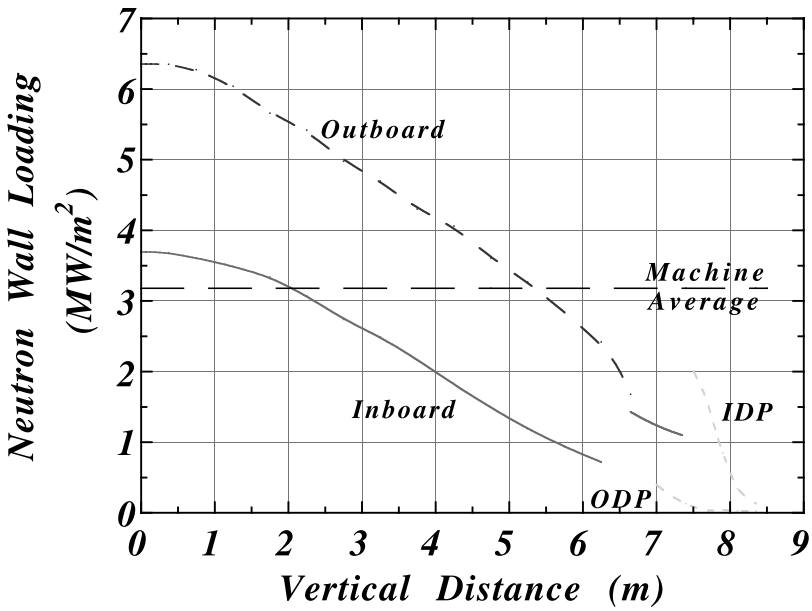

Fig. 2. Neutron wall load distribution (measured from mid-plane) IDP and ODP refer to inboard and outboard divertor plates.

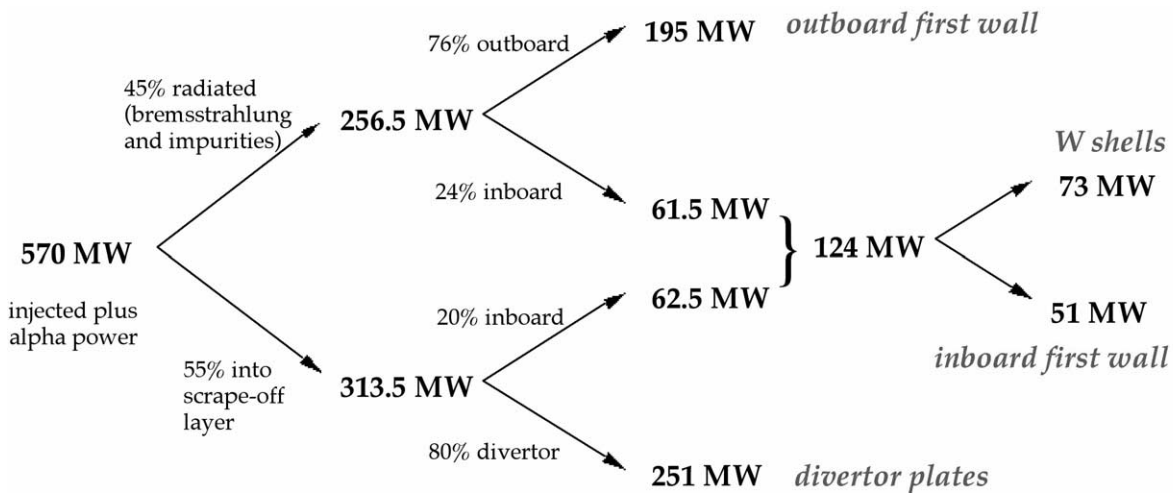

Fig. 3. Transport power flows.

vessel (which also serves as the TF return current leg), whereas Fig. 4 highlights the replaceable power core unit alone, sitting on top of its movable (reusable) support platform. The low-temperature components—the TF centerpost and PF coil shields—are physically independent from the high-temperature components.

The three major power core elements described here include: (1) the outboard breeding blanket and its first wall; (2) the inboard first wall and shield (including the inboard vertical stability shells); and (3) the divertors. These are assembled as an integrated unit outside the TF shell in 'hot cell' assembly and maintenance areas, and transported into place using a combination of rail and hydraulic lifting systems. All power core coolants enter and exit through the lower support platform [3]. This allows all maintenance connections to be made and broken outside the primary vacuum in a secondary containment area. Poloidal continuity is provided by the helium manifolds which surround the blanket and divertor, and are attached to the inboard first wall and shield. The manifolding, therefore, serves not only to route the two coolants but also to provide structural integration of the power core.

Single-piece construction of the power core is somewhat unusual for tokamaks; it is enabled in ARIES-ST by the elongated geometry of the plasma, the ability to provide electrical joints in the normal-conducting TF system, and the relatively modest drained weight of a self-cooled blanket (~ 768 T). Due to the modest replacement cost (~ $50 million), efforts to segment the blanket radially and/or re-use parts of the power core were not explored, although such techniques are possible, and could help reduce the waste stream considerably.

High thermal conversion efficiency combined with strong requirements on tritium control led to the choice of a helium Brayton power conversion cycle. For a Brayton cycle, high coolant outlet temperature is extremely important. In addition, low coolant inlet temperature influences the net cycle efficiency. Due to the restricted temperature window of ferritic steel, especially on the high end, the maximum He temperature is only 525 °C, which is not nearly enough to provide acceptably high thermal conversion efficiency. Fortunately, 80% of DT fusion power is in neutrons. Considering neutron heating in steel and other structures within the power core, about half of the total core power is removed in PbLi (see Table 1). The maximum PbLi temperature of 700 °C allows a maximum He temperature to the turbine of 680 °C, which enables a net cycle efficiency (including pumping power) of at least 45%. Helium inlet and outlet temperatures are designed to be equal in the blanket, divertor, and inboard

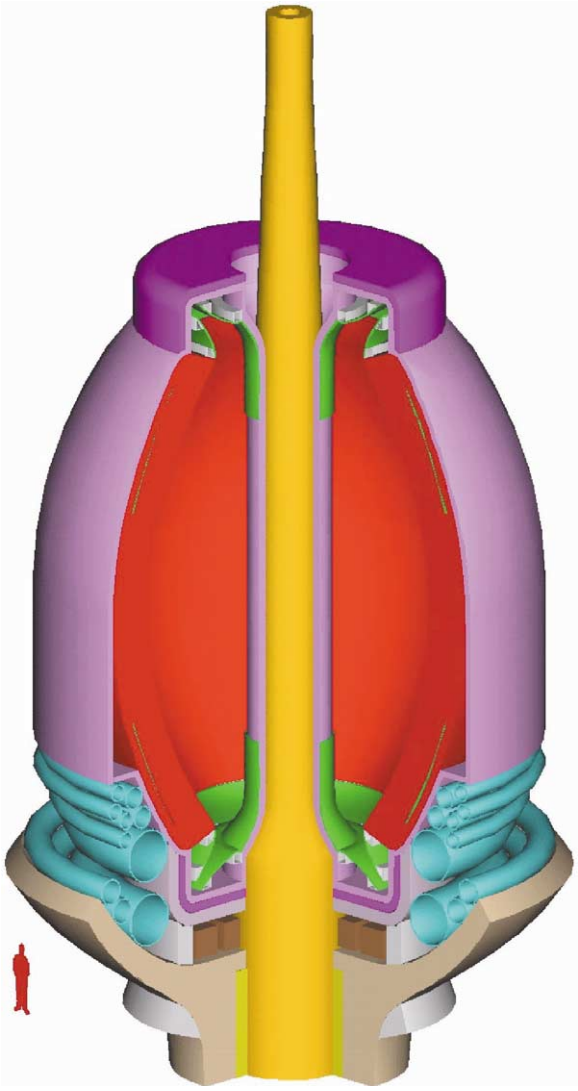

Fig. 4. Power core replacement unit.

Table 3
Power core temperatures

Inlet He temperature	300 °C
First wall exit temperature of He	379 °C
Blanket exit temperature of He	525 °C
Inlet PbLi temperature	550 °C
Exit PbLi temperature	700 °C
He temperature to the turbine	680 °C
Net cycle efficiency	≥45%

first wall and shield. Table 3 summarizes the coolant inlet and outlet temperatures.

In the remainder of this article, the design features and performance of the major power core components are described. Material issues and power core R&D needs are summarized at the end.

2. Outboard breeding blanket and first wall

2.1. Design selection

Self-cooled blanket configurations offer the best hope for simultaneously achieving high coolant outlet temperature and high power density. The combination of high power density (above 5 MW/m^2) with sufficiently high efficiency in the power conversion system cannot be achieved with solid breeder blankets irrespective of the structural material used, because the maximum temperature of all candidate breeder materials would exceed their operating limits.

Self-cooled lithium blankets with vanadium alloy as structural material allow for both high power density and high temperatures. However, they were avoided in ARIES-ST for safety reasons because water is used within the power core as the TF magnet system coolant. Safety concerns could be overcome by using the eutectic lead lithium alloy Pb–17Li instead of lithium. However, the heat transport properties as well as the compatibility with ferritic steels and vanadium alloys for this liquid metal are not as good as with pure lithium.

After surveying design options and considering the various design criteria, an advanced He-cooled ferritic steel blanket with flowing eutectic lead–lithium alloy Pb–17Li breeder was adopted. This design borrows features of both the EU dual-coolant DEMO blanket [11] and the PbLi-cooled SiC/SiC blanket 'TAURO' [12,13]. Several design modifications and performance enhancements were made to ensure compatibility with the ARIES-ST plasma and to allow it to meet the requirements for an attractive commercial power plant.

TAURO uses SiC/SiC composite as both structural and plasma-facing material. The electrical resistance of SiC/SiC, which is basically a semiconductor, is expected to be high enough to keep the MHD pressure drop within tolerable limits. While purely self-cooled designs retain a great appeal for their simplicity, several difficult problems arise using SiC/SiC as structural and plasma-facing material:

1) The large surface heat flux at the first wall requires a relatively high thermal conductivity in order to avoid excessively large temperature differences across the wall, leading to high thermal stresses.
2) The rather large stresses in the containing walls caused by the static pressure of PbLi and by disruption forces acting on the liquid metal have to be reacted by the composite material, which has very low ductility.
3) The use of the SiC/SiC composite as the structural material for a large pressure vessel with a complicated form requires the development of new fabrication methods—including novel joining techniques—which are compatible with liquid metal filling.

Problems associated with the use of SiC as a structural and pressure vessel material are avoided with the ARIES-ST dual-cooled blanket concept. Design changes to the blanket as compared with the EU–DEMO dual coolant design include extension of the power handling capability of the first wall by using an advanced ODS ferritic steel, use of thermally and electrically insulating SiC inserts instead of coatings to reduce the MHD pressure drop and also to ensure the steel structure remains within its design temperature limits while allowing a PbLi outlet temperature of 700 °C, optimization of the channel dimensions, and manifolding consistent with the temperature and design integration constraints.

2.2. Design description

A cross section of the outboard breeding blanket is shown schematically in Figs. 5 and 6. The blanket consists of a helium-cooled ferritic steel first wall with toroidal coolant paths, poloidally-oriented liquid metal ducts defined by internal grid plates, and manifolding.

The use of ferritic steel as a first wall material leads to concerns over ferromagnetic effects, including forces on structures and magnetic interactions with the plasma. The level of detail needed to properly analyze these interactions was considered beyond the scope of this study, and therefore, these concerns were left as candidates for future consideration.

A cross section of the first wall is shown in Fig. 7. The first wall box is fabricated by diffusion welding and subsequent bending of the straight plates containing the milled coolant channels [11]. The resulting array of 'I-beams' creates stiffness against toroidal bending. This first wall forms, together with the helium manifolds at the back side of the segment, a box containing the flowing liquid metal breeder.

The design of the first wall and blanket was heavily influenced by the desire for high reliability. For example, there are no welds through the first wall thickness. The diffusion welds are between parallel channels with little or no differential coolant pressure and little or no consequence of a local failure. The first wall box is welded into the manifolds along the back side where the stresses are low and the radiation flux is attenuated and softened. Low coolant pressure leads to low primary stresses. Overall, many design features were incorporated to ensure low failure rates and minimal consequences in case of failure.

One-sided roughening of the coolant channels (on the side nearest the plasma) increases the heat transfer coefficient to the coolant, which lowers the structure peak temperature and temperature variations. Since only one of the four walls in a channel is roughened, the increase in pressure drop is modest.

A grid of steel plates inside this box creates large liquid metal ducts and reinforces the first wall box, providing stiffness against poloidal bending. They are also fabricated by diffusion welding, similar to the first wall, and are internally cooled by helium.

Flow channel inserts made of silicon carbide are placed inside the liquid metal ducts (see Fig. 8). These inserts serve as electrical and thermal

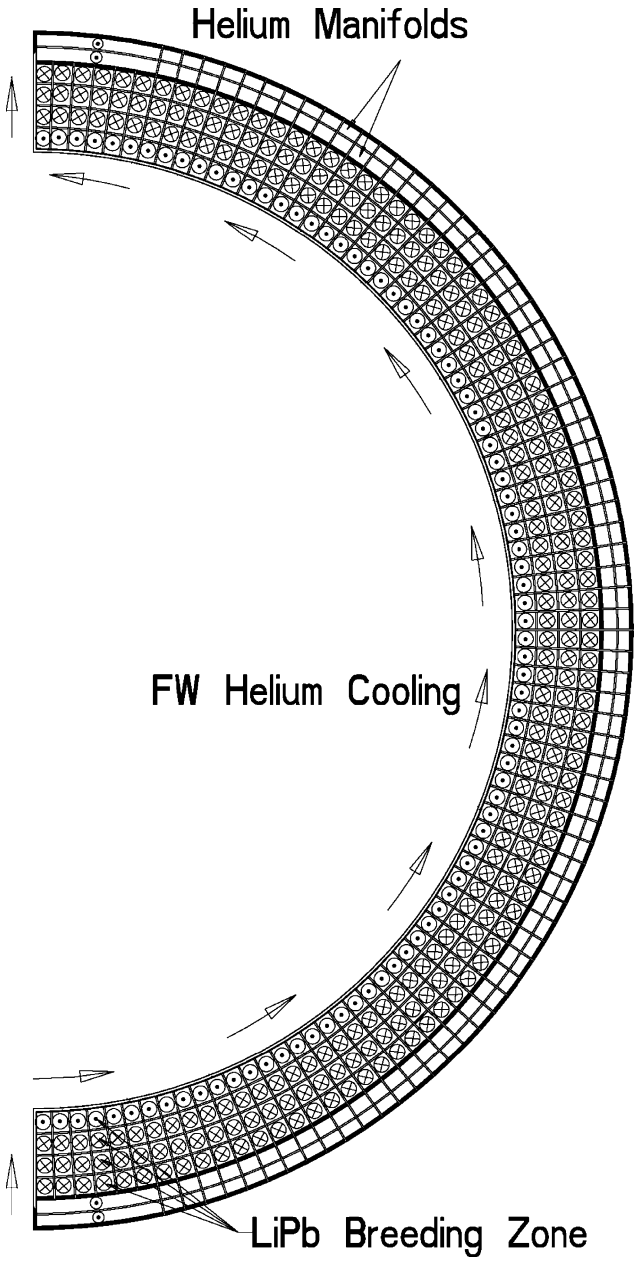

Fig. 5. Outboard blanket cross-section.

insulators between the flowing liquid metal and the steel structure. In order to equilibrate pressures and hence reduce stresses on the SiC, an opening is located along the back side and a small gap is provided between the SiC insert and the surrounding walls. A single opening to the electrically conducting structures is expected to have little or no effect on the MHD flow behavior and pressure drop.

A thermal conductivity of at least 15 W/m K is usually required to avoid excessively large temperature differences across the first wall. However,

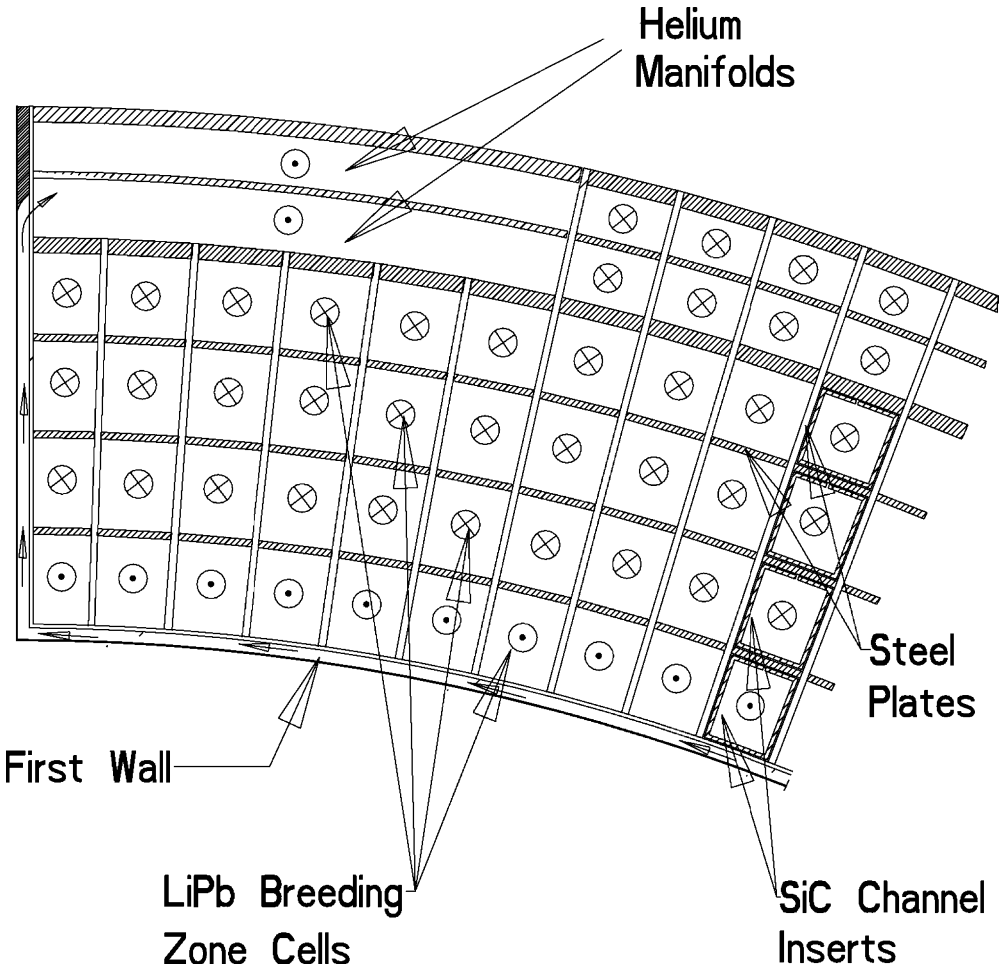

Fig. 6. Detail of blanket cross-section.

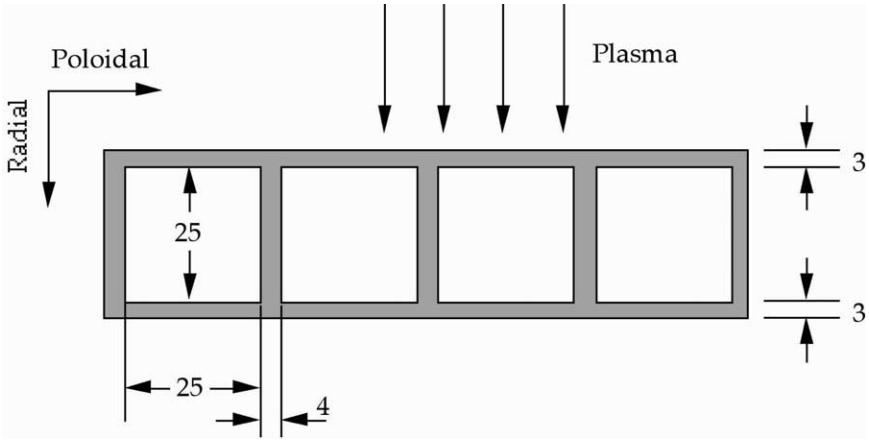

Fig. 7. Cross section of the first wall box.

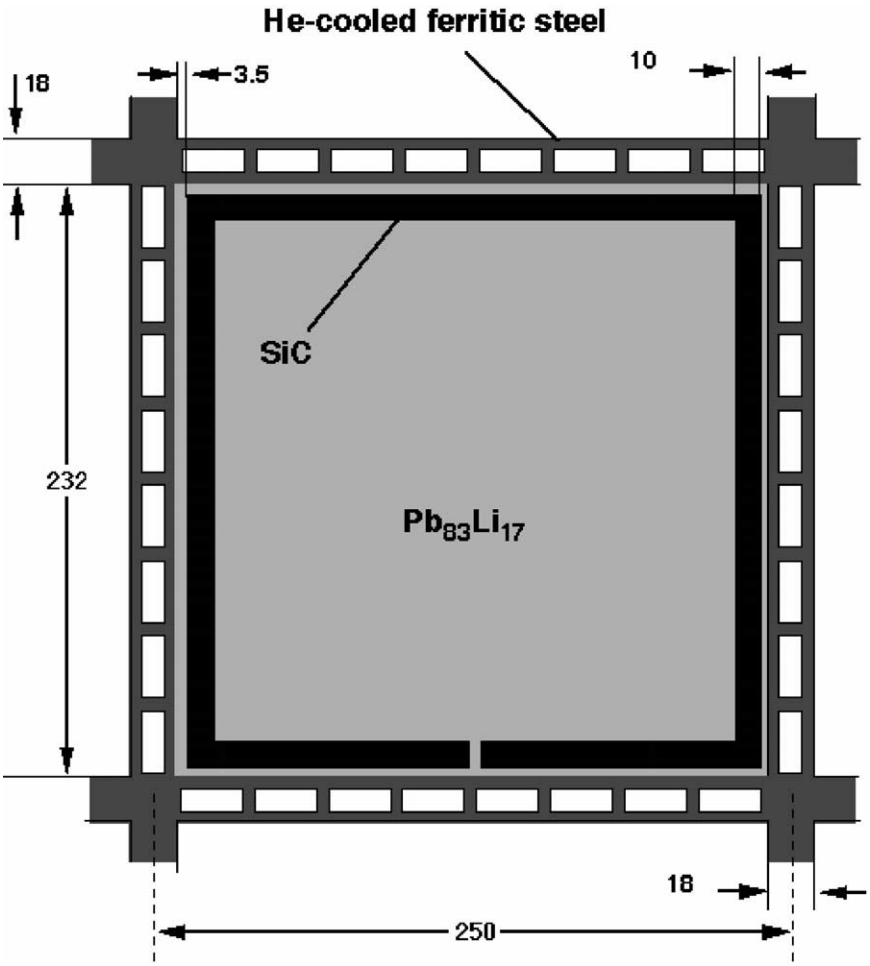

Fig. 8. Cross section of the breeder region unit cell.

for the design proposed here, the first wall heat flux does not pass through SiC. A thermal conductivity as low as possible is required because the material serves here as an insulator. A value of 4 W/m K has been assumed. It should be possible to achieve such a low value with simple 2-D composites.

Blanket designs based on the use of SiC/SiC as a pressure container have been criticized frequently because it has low ductility and is uncertain as a leak-tight container. Both aspects—the integrity under mechanical load and the leak tightness—are much less important for the design proposed here because the SiC serves only as an insulator. Any mechanical loads from the coolant pressure are avoided by pressure equalization between the flowing liquid metal and the stagnant zone at the outer side. Therefore, it may be possible to use solid SiC or at least the most simple 2-D composite to reduce cost decisively.

The Pb–17Li breeder enters the blanket at the bottom, flows upward in the front row of ducts, turns around at the top by 180° and flows downward in the two parallel rows at the rear of the blanket. In this design, a liquid metal exit temperature of about 700 °C is achievable, allowing either an advanced Rankine steam cycle or closed-cycle helium gas turbine (Brayton cycle) power conversion. A gross thermal efficiency of about 45% can be achieved with either system.

The manifold geometry in ARIES-ST is rather complex, but is designed to provide several important functions (i.e. shielding and mechanical integration as well as coolant routing) with high reliability [14]. The helium manifolds are an integral part of the blanket box. Separate welds are not required between each cooling channel and the manifolds, which is expected to increase reliability.

The incoming helium at 300 °C first cools the first wall and then the grid plates, where it is heated up to 525 °C. Flowing in series means lower temperatures in the first wall and higher coolant temperatures in regions with lower power density, minimizing temperature differences in the blanket structure. The blanket helium flow is further subdivided into two independent counter-flowing systems. The cooling channels in the first wall as well as those in the grid plates are alternately connected to one of the two systems in order to minimize the temperature increase in case of a loss-of-coolant accident (LOCA) in one of the systems. Another benefit of the alternating flow directions is the more equal temperature distribution in the entire segment, resulting in lower thermal stresses. The temperature of the steel structure is maintained everywhere below 600 °C.

Due to the high PbLi outlet temperature, special considerations are needed for the pipes leading to the power conversion system. A characteristic feature of Pb–17Li is its low tritium solubility. The resulting high tritium partial pressure can lead to intolerably high tritium permeation losses from the coolant access tubes, and therefore, generally requires additional permeation barriers. Another issue is the choice of materials. There is no available steel that will allow a temperature above 600 °C. To solve both problems, concentric access tubes are used with the liquid metal flowing in the inner tube and helium in the annular gap. In this way, helium with a temperature of 500 °C cools the liquid metal duct, especially if a thermal insulator is arranged inside the liquid metal tube. About 15-mm thick SiC is proposed for this purpose. This design allows the use of steel for all access tubes. Tritium from the Pb–17Li in this case will not enter the building atmosphere but rather the helium coolant, where it can be recovered easily.

One main argument against the use of Pb–17Li blankets has been the radiotoxity of ^{210}Po. Investigations performed in Europe during the past 5 years, however, showed that this problem had been vastly overestimated [11]. More precise neutronic data as well as more adequate calculation methods indicate ^{210}Po generation is orders of magnitudes lower than previously estimated. Release experiments of ^{210}Po from Pb–17Li proved that the release rates are not determined by the vapor pressure of Po but rather by the vapor pressure of a Po–Pb compound which is orders of magnitude lower than that of the element itself. Both effects—the lower ^{210}Po generation and the lower release rates—led to the conclusion that ^{210}Po is no longer a significant safety issue. For a typical case, the contribution of ^{210}Po to the total dose to the public during a LOCA has been estimated to be less than 1%. The total release of radiotoxic materials was in any case so small that no evacuation of the public would be required.

2.3. Thermal–hydraulics

One of the fundamental requirements on the first wall and blanket is to remain within allowable temperature and stress limits during exposure to normal plasma operation. Ferritic steel is known to be limited in its temperature and stress handling capability by a relatively constrained temperature window and unimpressive thermal conductivity (which leads to high temperatures gradients, increasing both peak temperature and thermal stress). On the low temperature end, concerns over loss of ductility under irradiation suggests a lower limit of 300–350 °C [15]. Lower temperatures are acceptable if design stresses can be maintained low enough to meet design codes for embrittled materials. However, for the sake of conservatism, we chose to operate all pressure-vessel structures above the anticipated ductile-to-brittle transition temperature (DBTT).

On the high-temperature end, reduced yield strength and thermal creep limit conventional ferritic steel alloys to approximately 550 °C (depending on stress levels and design rules). This

upper temperature limit impacts not only the ability to withstand high surface heat flux, but also our ability to operate the gas Brayton cycle with acceptable conversion efficiency. Recent studies suggest that higher-temperature ferritic steels, such as oxide dispersion strengthened (ODS) variants, may be feasible for fusion service conditions [16–19]. If the upper temperature can be increased to 600 °C without commensurate increase in the lower limit DBTT, then an acceptable operating margin is possible for the ARIES-ST first wall design. This maximum temperature occurs only at the outermost surface of the plasma-facing wall; the through-thickness average is below 550 °C. Depending on the exact value of stress and the appropriate design rules for the first wall, a peak surface temperature of 600 °C may be possible even without the use of more advanced alloys (see Section 5).

For self-cooled blankets, withstanding volumetric heating is not usually a major concern. For the ARIES-ST dual-cooled blanket, the MHD pressure drop should be much lower than conducting wall designs due to the use of insulating inserts. However, detailed MHD analysis was not performed to estimate 3-D entrance and manifolding effects, which could substantially affect the flow patterns and total pressure drop. Besides incurring locally large pressure drops, hot spots in the breeder could result if the flow is affected by MHD interactions. Better multi-dimensional modeling tools are needed in order to examine complex geometric effects accurately.

Peak temperatures and stresses are expected to be more severe in the plasma-facing region, which is cooled by helium. Here volumetric heating has a significant, but secondary impact. Therefore, the primary focus of thermal–hydraulic analysis was to determine the maximum allowable surface heat flux.

2.3.1. Design parameters

The final ARIES-ST design point has an average surface heat flux of 0.46 MW/m^2 in the outboard first wall. The peak surface heat flux depends on several factors, including core impurity and divertor radiation distributions. Assuming most of the core impurity radiation takes place near the outermost flux surfaces, peaking on the outboard first wall is due mainly to bremsstrahlung radiation (which peaks near the mid-plane) and the radiative divertors (which peak away from the mid-plane). Fig. 9 shows the bremsstrahlung radiation distribution along the first wall, with a peak-to-average value of 1.3. The W stabilizing shells act as a high-heat flux transition region capable of handling at least 2 MW/m^2 of surface heating that might result from the localized divertor radiation heat source.

A goal surface heat flux capability of 0.8–0.9 MW/m^2 on the steel first wall was chosen based on a combination of safety factors and uncertainties. Since previous ferritic steel blanket designs (such as the dual-coolant EU–DEMO design) have not been pushed beyond a surface heat flux of $\sim$0.5 MW/m^2, extension of the surface heat flux handling capability was considered important for the success of ARIES-ST.

The channel dimensions were established by considering several factors, including mechanical stiffness, stress limits, thermal–hydraulic and neutronic considerations. Table 4 summarizes these and other key first wall parameters. The key dimensions include the first wall thickness, the second wall thickness, and the channel radial depth. The yield strength of the structural material restricts the size of the coolant channels and the minimum thickness of the first wall. Pressure in the coolant channels creates membrane and primary bending stresses that limit how thin the first wall

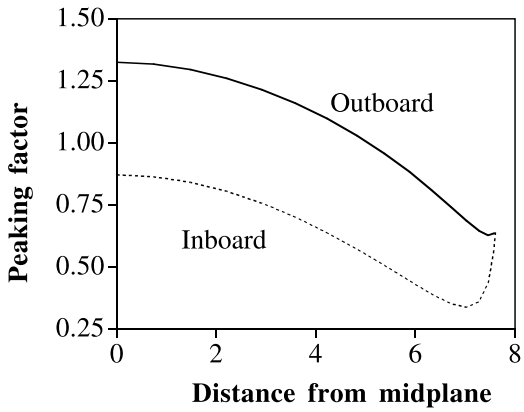

Fig. 9. Bremsstrahlung surface heat flux distribution on the first wall.

Table 4
First wall parameters used for thermal–hydraulic and stress analysis

First wall thickness, δ_1	3 mm
Second wall thickness, δ_2	3 mm
Web thickness, w	4 mm
Span between grid plates, L	25 cm
First wall channel depth, a	25 mm
Roughness of ribbed surface, ε/a	0.0018
Roughness of smooth surfaces, ε/a	0.0018
Coolant pressure, p	12 MPa
Coolant velocity, v	75 m/s
Steel properties	
Thermal conductivity, k_s	26.2 W/m K
Young's modulus, E	207 GPa
Poisson's ratio, ν	0.3
Thermal expansion coefficient, α	12×10^{-6} K^{-1}

can be. The heat flux and temperature difference across the first wall set up thermal secondary stresses that limit the heat flux and how thick the first wall can be.

A 25-mm channel depth with a 5-mm first wall thickness was used for the EU–DEMO dual-coolant design, and was studied extensively with detailed stress analysis [20]. This depth provides adequate bending stiffness and also leads to acceptable pressure drop and bulk temperature rise for a straight-through coolant path. Parametric studies showed that a 20% increase in heat transfer coefficient could be obtained by reducing the channel size. However, the reduced bending strength is a concern in the event of an internal coolant leak leading to module pressurization.

The peak bending stress in an I-beam, which is a good representation of the first wall construction (see Fig. 10), can be approximated by:

$$\sigma_{\max} = \frac{p}{12}\frac{L^2}{at}, \tag{1}$$

where p is the internal pressure; L, the span length (between grid plates); a, the channel depth; and t is the wall thickness. For the higher coolant pressure used in ARIES-ST, a very small span length is required to maintain acceptable bending stresses.

The total amount of steel in this first wall design, in combination with the presence of SiC inserts and the absence of an inboard breeding blanket, led to marginal tritium breeding ratio. In the final design, the wall thicknesses were reduced to 3 mm in order to allow adequate breeding, as well as to extend the thermal–hydraulic limits. The net result is the inability of the first wall to withstand an internal blanket coolant rupture. Instead, rupture disks are used to prevent first wall failure in the event of an internal blanket failure.

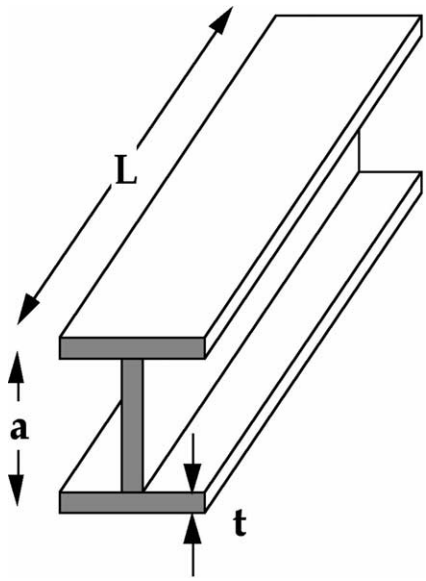

Fig. 10. The first wall approximated as an I-beam.

2.3.2. Analysis of the first wall region

The thermal–hydraulic heat flux limit is most easily understood in terms of the temperature window of operation. A 'temperature budget' exists due to the upper and lower temperature limits of the steel. The coolant inlet temperature, $T_{\text{in,He}}$, must be at least equal to the minimum allowable structure temperature. Considering the bulk coolant temperature rise, film drop and gradient through the first wall, the temperature budget is expressed as follows:

$$T_{\text{max,steel}} - T_{\text{in,He}} = \Delta T_{\text{bulk}} + \Delta T_{\text{film}} + \Delta T_{\text{fw}}. \tag{2}$$

In both the EU DEMO blanket with $T_{\text{max,steel}} = 550$ °C and $T_{\text{in,He}} = 250$ °C and ARIES-ST blan-

ket with $T_{max,steel} = 600$ °C and $T_{in,He} = 300$ °C, the temperature budget is 300 °C.

For the dual-coolant ARIES-ST design, the bulk temperature rise in the first wall is further constrained by compatibility with the other plant power flows and the power conversion system. The overall plant power fraction carried by high-temperature He coolant is 48% (see Table 2), corresponding with a blanket He outlet temperature of 525 °C. With about 35% of the bulk temperature rise in the first wall and 65% in the grid plates, the bulk temperature rise in the first wall is 79 °C, corresponding to an outlet temperature of 379 °C.

Using this bulk temperature rise, the remaining temperature budget for the film drop and wall conduction is:

$$\Delta T_{film} + \Delta T_{fw} = \frac{q}{h} + \frac{q\delta}{k} = 221\ ^\circ\mathrm{C}. \tag{3}$$

The maximum allowable heat flux is plotted in Fig. 11 as a function of flow speed for a channel width of 2.5 cm and a first wall thickness of 3 mm. Any point on or below the dashed line is a case where the maximum steel temperature will not exceed 600 °C. In all cases, enhancement of the convective heat transfer coefficient by a factor of two is obtained through the use of low transverse grooves on the plasma-facing side of the cooling channels [21,22].

Pumping power (P_p) in the first wall is used as an additional constraint. Values in the range of 5–10% of the thermal power (P_t) removed are not unreasonable for a high heat flux component, in which some economic penalty is considered reasonable in order to accommodate higher power density. Results indicate a relatively minor gain in heat transfer as the pumping power is allowed to rise from 5 to 10%. Using $P_p/P_t = 5\%$:

$$q = 10 v^3 f \rho_{He}, \tag{4}$$

where f is the friction factor, adjusted for one-sided surface roughening.

Eq. (4) is also plotted in Fig. 11. Staying above the pumping power curve and below the steel temperature curve, an eye-shaped zone is created. It is within this zone that the blanket must operate to meet the temperature and pumping power restrictions. The maximum allowable heat flux is well above 1 MW/m^2. This indicates that thermal–hydraulic performance does not limit the heat flux.

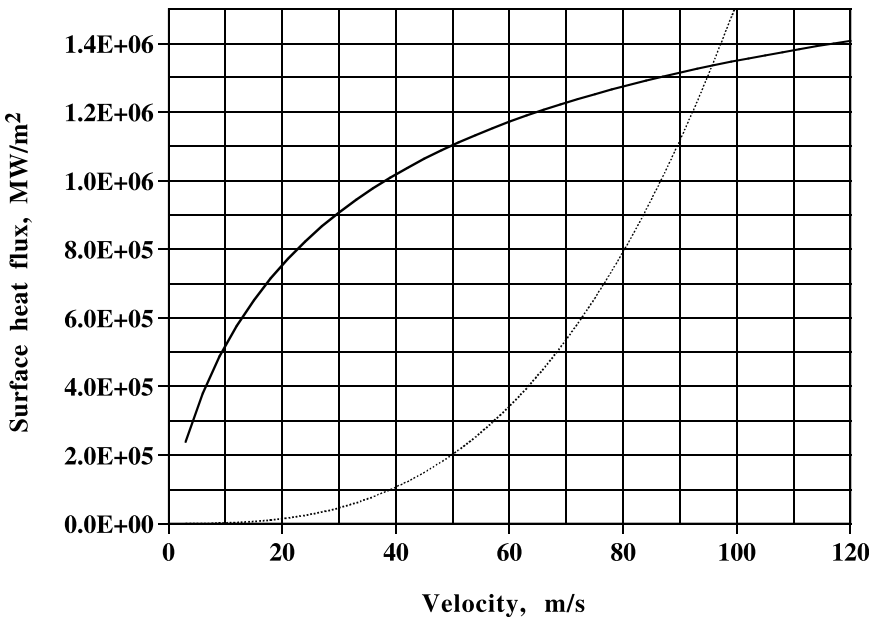

Fig. 11. Heat flux window of operation in the outboard first wall.

Thermal stresses, as shown in the following section, are more limiting.

If we fix $\Delta T_{bulk} = 79$ °C, then the length, L, of the duct can be calculated from the definition of the bulk temperature rise:

$$\Delta T_{bulk} = \frac{\dot{q}L}{\rho_{He} a v c_p}, \quad (5)$$

For a 25-mm duct and 75 m/s coolant velocity, the self-consistent path length is approximately equal to half the circumference of the power core at mid-plane.

2.4. Stress analysis

Stress analysis was performed in 2- and 3-D using ANSYS [23] in order to determine the maximum allowable surface heat flux for the reference design (25-mm channel with 3-mm first wall). In accordance with the ASME pressure vessel code [24], 'level A' loading allowables were used as follows:

1) allowable membrane primary stress: 1 S_{mt};
2) allowable membrane + bending primary stress: 1.5 S_{mt};
3) allowable primary + secondary stress: 3 S_m.

with $S_m = \min((2/3)\sigma_{0.2}, (1/3)\sigma_u)$ and $S_{mt} = \min(S_m, (2/3)\sigma_{R,t}, (1/3)\sigma_{1,t})$, where $\sigma_{0.2}$ is the 0.2% offset yield stress, σ_u is the tensile strength, $\sigma_{R,t}$ is the creep resistance, $\sigma_{1,t}$ is the 1% creep strain limit, and t is the time to failure, with $t = 2 \times 10^4$ h for end of life.

Design allowables from [20] for 1.4914 steel (MANET) and suggested allowables for ODS steel are given in Table 5. The design allowables for ODS are assumed to have an advantage of 50 °C over MANET, so the values for MANET are simply shifted up by 50 °C.

Fig. 12 shows the temperature distribution resulting from a 0.95 MW/m^2 uniform surface heat flux and convective heat transfer coefficient of 16 720 W/m^2 K at the plasma facing wall (8360 W/m^2 K for the other walls), which corresponds with a helium velocity of 125 m/s. The bulk temperature is 400 °C.

Representative boundary conditions are crucial to obtaining accurate results for this simplified geometric model. The model uses one and a half channels with the positive-x and positive-z faces subject to a symmetry boundary condition (bending and displacement constrained only in the z-direction). No constraints are imposed on the back ($-z$) and left ($-x$) faces. In addition, no constraints are applied on the top face ($+y$), whereas the bottom ($-y$) is constrained in the y direction at $-z$ (making it a 167-mm beam between grid plates). This model results in large apparent deformations in the left wall which are an artifact of the boundary conditions. The results are used only from the I-beam located on the right side of the model. Extensive benchmarking against the EU-DEMO design showed that the results of this simplified model were within 30% of the more complete analysis.

Table 6 summarizes the stress analysis results. Fig. 13 shows the pressure stress and Fig. 14 shows the thermal plus pressure stresses for the base case. All stress results presented here are von Mises stresses. The peak primary stress (at the plasma facing wall) is about 70 MPa. Note, for this analysis, 8 MPa was used for the coolant pressure, whereas the final design point adopted 12 MPa pressure for compatibility with the inboard first wall and divertor plates.

The primary membrane condition applies in the web where the maximum stress is 68 MPa and the temperature 500 °C. This is well below the 1 $S_{m,t}$ limit of 183 MPa for ODS steel and is below the 1 $S_{m,t}$ limit of 165 MPa for MANET. The membrane plus bending condition applies at the first wall where the highest stress is 148 MPa at 580 °C. This is well below the 1.5 $S_{m,t}$ limit of 195 MPa for ODS steel, but does not meet the limit of 100 MPa for MANET. Therefore, the proposed design meets the first two criteria for ODS steel, but not MANET.

Fig. 14 shows the von-Mises stress distribution in 3-D for the combined pressure and thermal loading. The highest stress occurs in the first wall and is 430 MPa at a temperature of 575 °C. This is below the 3 S_m limit of 464 MPa for ODS steel but does not meet the 398 MPa limit for MANET.

Table 5
Design stress allowables for MANET and postulated advanced ODS alloy

Temperature (°C)	MANET		ODS	
	S_m (MPa)	$S_{m,t}$ (MPa)[a]	S_m (MPa)	$S_{m,t}$ (MPa)[a]
20	258	258	–	–
50	258	258	258	258
100	256	256	258	258
150	252	252	256	256
200	246	246	252	252
250	237	237	246	246
300	227	227	237	237
350	215	215	227	227
400	200	200	215	215
450	183	183	200	200
500	165	165	183	183
550	144	98	165	165
600	121	41	144	98

[a] At $t = 2 \times 10^4$ h.

The proposed design meets all of the ASME criteria for ODS steel.

The proposed helium-cooled, 3-mm first wall using 25-mm square channels with heat transfer enhancement of the plasma facing wall can theoretically remove 0.95 MW/m^2 according to both thermohydraulic and thermomechanical analysis. Use of ODS steel instead of MANET allows the design to withstand a higher heat flux due to higher creep strength and yield strength.

The design is able to withstand the 0.95 MW/m^2 heat flux from a thermomechanical standpoint, depending on the fidelity of the thermal-stress analysis results. Comparing the results of the ANSYS models to the work in [20] for EU–DEMO, the stress distribution of the models are

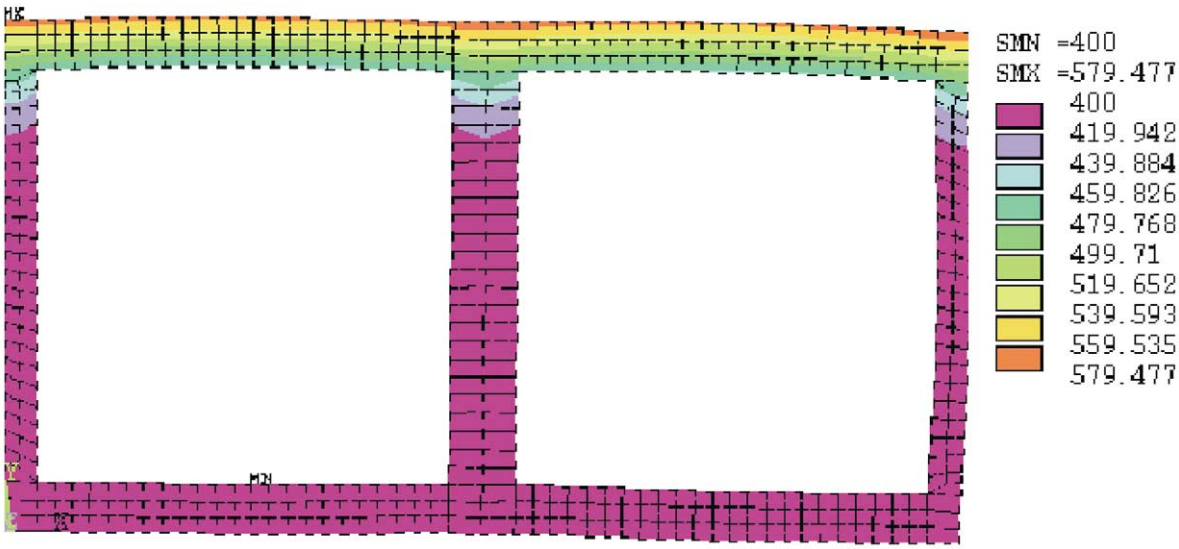

Fig. 12. Temperature distribution in the first wall.

Table 6
Thermomechanical results for the first wall at 0.95 MW/m^2

Design condition	Temperature (°C)	Calculated peak value (MPa)	Code limit (MPa)
Membrane stress (in web)	500	68	183
Membrane plus bending	580	148	195
Primary plus secondary	575	430	464

different, but are of similar magnitude for minimum and maximum values. The two models differ by about 30%, but this is considered good agreement since the ANSYS models used far fewer elements than the work in [20].

Two-dimensional plane strain elements are fairly good at describing the stresses due to only internal pressure. Results are consistently within 25% of 3-D values and are conservative, since the 2-D plane strain is like a 3-D model constrained in one axis. Off-normal pressures induce bending which requires 3-D analysis. The same can be argued for thermal loads which should only be applied when using 3-D analysis. The plane strain behavior of the 2-D model is over-constraining in thermal analysis and pushes the stresses up an order of magnitude over the actual stress values that are found in 3-D analysis.

Irradiation creep and swelling were estimated by considering the location of maximum membrane stress. The maximum linear swelling strain is $\leq$ 2.25% and the maximum irradiation creep strain is $\leq$2.24%, both evaluated at a fluence of 150 dPa [25,26]. The bending stress causes no net change in shape. Rather, irradiation creep relaxes the bending component of stress as it causes positive and negative changes in strain in the plane of the first wall across the thickness. These average out to zero with regard to net deformation outward or inward.

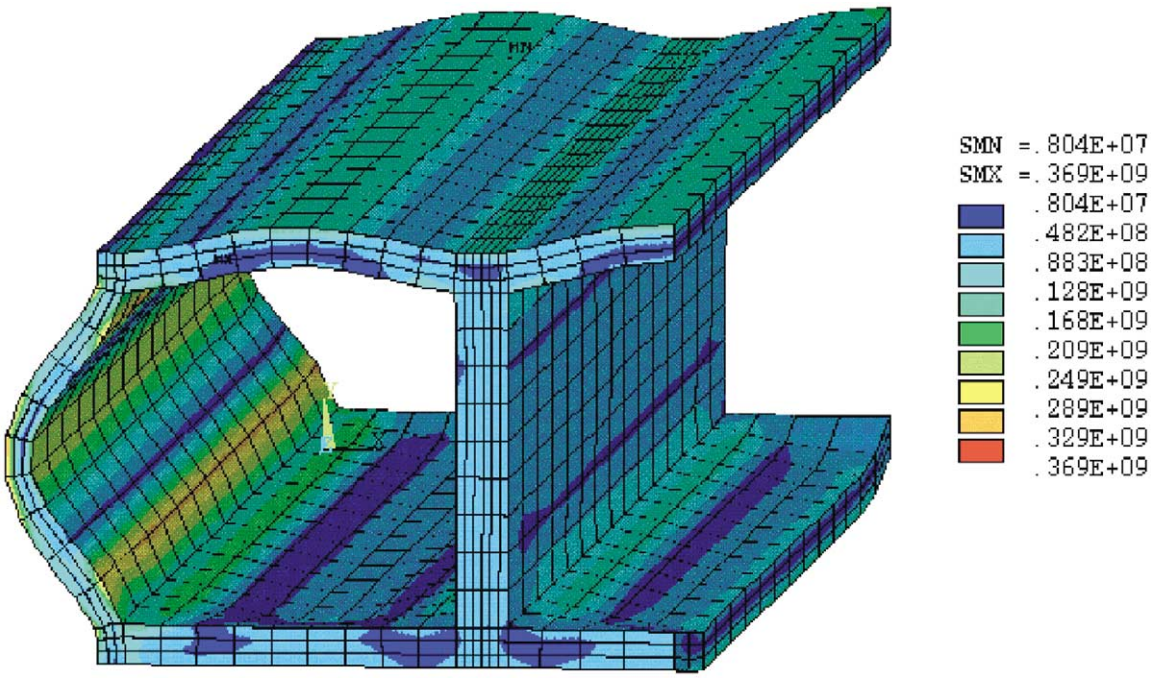

Fig. 13. First wall pressure Von Mises stresses (S_m or 1.5 S_{mt} limit).

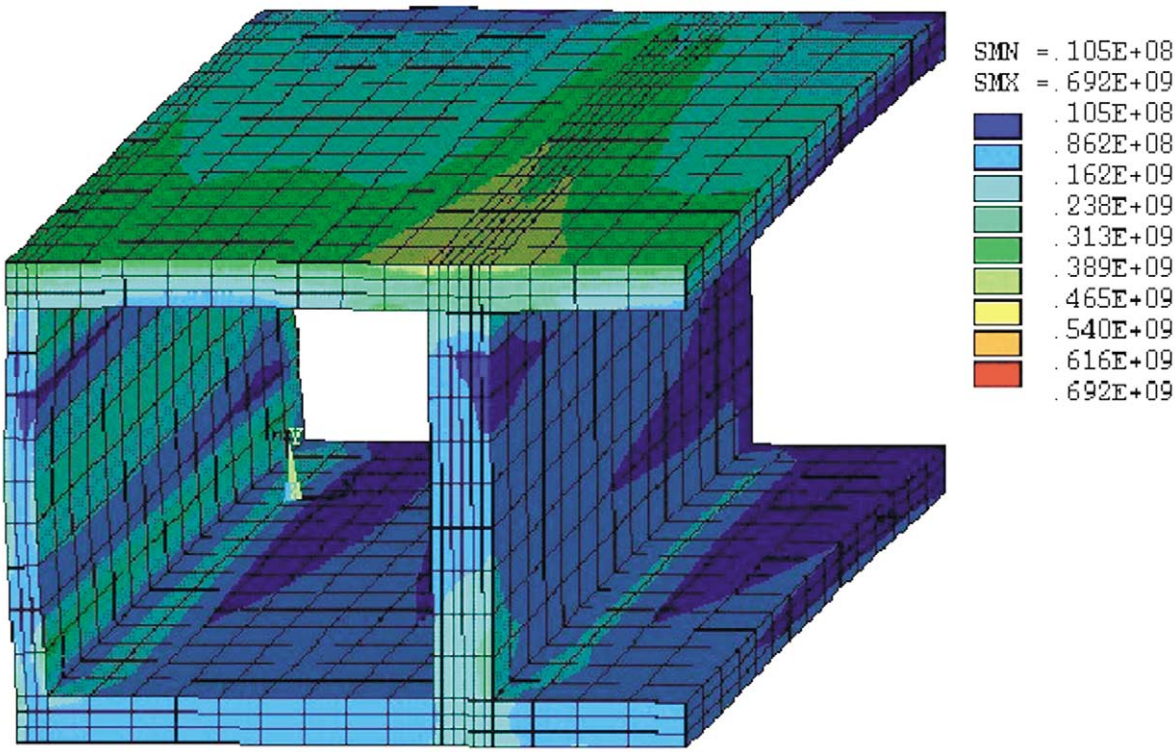

Fig. 14. First wall thermal plus pressure Von Mises stress (3 S_m limit).

Irradiation creep and swelling are not associated with material failure in the same way that thermal creep is. There is no ductility limit associated with these deformation mechanisms; they must be accounted for in designs to accommodate the resulting deformation. Typically, an approximate design limit of 5% is chosen. Based on these rough estimates, we believe these levels of deformation could be accommodated in the design.

2.5. Power conversion

Recirculating power in a normal-conducting TF coil system can be very high; early estimates were as high as 75% of the net electric power. In the final optimized ARIES-ST design point, the recirculating power is about half of the net electric power. While an exact target can not be specified, thermal conversion efficiency should be as high as possible to offset this effect. For example, Fig. 15 shows the relationship between the thermal conversion efficiency, recirculating power fraction and net plant efficiency for 1000 MWe net electric output.

A distinguishing feature of the power conversion system for ARIES-ST is the use of two coolants:

1) a helium loop with an inlet temperature of 300 °C and an outlet temperature of 525 °C;
2) a liquid metal loop with an inlet temperature of 550 °C and an outlet temperature of 700 °C.

These heat sources can be used either for a Rankine cycle (steam turbine) or for a Brayton cycle (closed-cycle gas turbine). A gross thermal efficiency of at least 45% can be achieved with both power conversion systems based on the temperatures listed above. A closed cycle helium gas turbine process was chosen as the reference concept for the following reasons [27]:

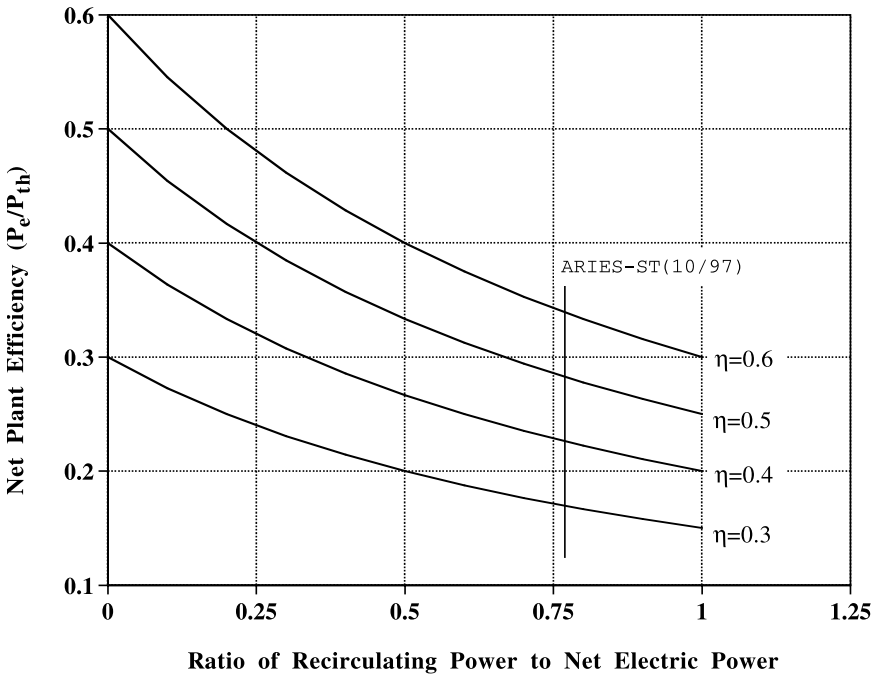

Fig. 15. Relationship between thermal conversion efficiency, recirculating power and net plant efficiency.

1) a steam turbine cycle has little potential for further improvement of the efficiency. To achieve a value of 45%, already an advanced system with a steam pressure of 31 MPa and two reheats to 565 °C is required. A helium gas turbine cycle with a maximum pressure of 18 MPa can lead to the same efficiency at a maximum helium temperature of 650 °C. A rise of this temperature looks feasible and would increase the efficiency substantially.
2) Liquid metal–water heat exchangers are always a safety concern. Those concerns are mitigated by the use of the less reactive alloy Pb–17Li but the acceptance of liquid metal cooling can be greatly enhanced if the potential for a liquid metal–water reaction is avoided.
3) Tritium permeation losses from the Pb–17Li through the heat exchanger tube wall can be much more easily recovered from helium than from water.
4) There is much higher flexibility for the selection of structural materials for the components outside the irradiation environment if inert helium is used.
5) Liquid metal with a temperature of 700 °C may require the use of refractory metals in the heat exchanger. Those metals are always endangered by water leaks becoming a source of oxygen in the system. In a system without water in the high temperature components the helium can be purified to a much higher degree.

A high compression ratio is required to allow for the relatively low helium temperature of 300 °C. The temperature differences available in both systems will result in reasonably small heat transfer surface areas in both types of heat exchangers.

The parameters for the ARIES-ST power cycle design are summarized in Table 7. The thermal power distribution was calculated using detailed neutronics calculations and surface heat fluxes coming from both radiation and transport power. The temperatures of each coolant have been

Table 7
Parameters for the ARIES-ST power conversion system

Total fusion power	2859 MW
Total thermal power	3107 MW
First wall and divertor plate	674 MW
Outboard blanket	1944 MW
Inboard shield	288 MW
Divertor shield	201 MW
Coolant load	
For He	
First wall and divertor plate	674 MW
Outboard blanket	553 MW
Inboard and divertor shield	489 MW
Total in He	1716 MW
For Pb–Li	1391 MW
He temperature	300–525 °C
He pressure	12 MPa
Pb–Li temperature	550–700 °C
He flow rate	1444 kg/s
Pb–Li flow rate	47 450 kg/s
Pb–Li velocity	
In ring header	3 m/s
In front blanket zone	0.67 m/s
In back blanket zone	0.21 m/s
He temperature to turbine	300–680 °C
Cycle efficiency	45%

selected to be the most efficient combination for the power conversion system, and are consistent with the design of the blanket, first wall, center column and the divertor. The coolant temperatures are limited by the structural materials selected, i.e. ferritic steel and SiC. Also, the interface temperature between static Pb–Li and steel is limited by the possible corrosion concerns. For this reason, it is important to match the two coolant temperatures so that the pinch point will not be a limiting factor for the power conversion.

Fig. 16 shows the T–H (temperature–enthalpy) diagram for the heat exchange between the He coolant and the Pb–Li. To obtain a high He exit temperature from the Pb–Li–He heat exchanger, the following considerations are included:

1) the most important design consideration is to have the maximum possible He exit temperature from the blanket, and also maximum possible Pb–17Li inlet temperature to the blanket. This can avoid a possible pinch point temperature limitation, which will reduce the achievable He temperature to the power conversion system. The maximum He exit temperature from the blanket is limited by the temperature limitation of the steel. Careful design concluded that a temperature range of 525–550 °C is possible. For the final design, a He temperature of 535 °C was selected. The inlet Pb–17Li temperature of 550 °C was selected to provide a temperature difference of 25 °C for the design of the Pb–17Li to He heat exchanger.
2) To maximize the He temperature to the turbine with a fixed pinch point temperature, the He inlet temperature to the blanket has to be moderately low. With a He inlet temperature of 300 °C, a He temperature of 680 °C can be reached. This is the optimum temperature range for the power conversion system.

In order to get the highest efficiency and to avoid pinch point problems, there is no heat exchanger between the primary and secondary helium; in other words, the same He flowing through the power core (possibly containing radioactive impurities) also passes through the turbines and compressors. The He pressure in the blanket is necessarily the same as the pressure at the turbine inlet.

The power conversion efficiency of a closed cycle gas turbine has been extensively studied. The efficiency for a cycle with three compressor stages can be calculated by the following equation:

$$\eta = \frac{\eta_t\,(T_o/T_s)[1-\beta(1/r)^{\gamma-1/\gamma}] - (3/\eta_c)(r^{\gamma-1/3\gamma}-1)}{(1-\eta_x)[(T_o/T_s)-1-(1/\eta_c)(r^{\gamma-1/3\gamma}-1)] + \eta_x\eta_t T_o/T_s[1-\beta(1/r)^{\gamma-1/\gamma}]}, \tag{6}$$

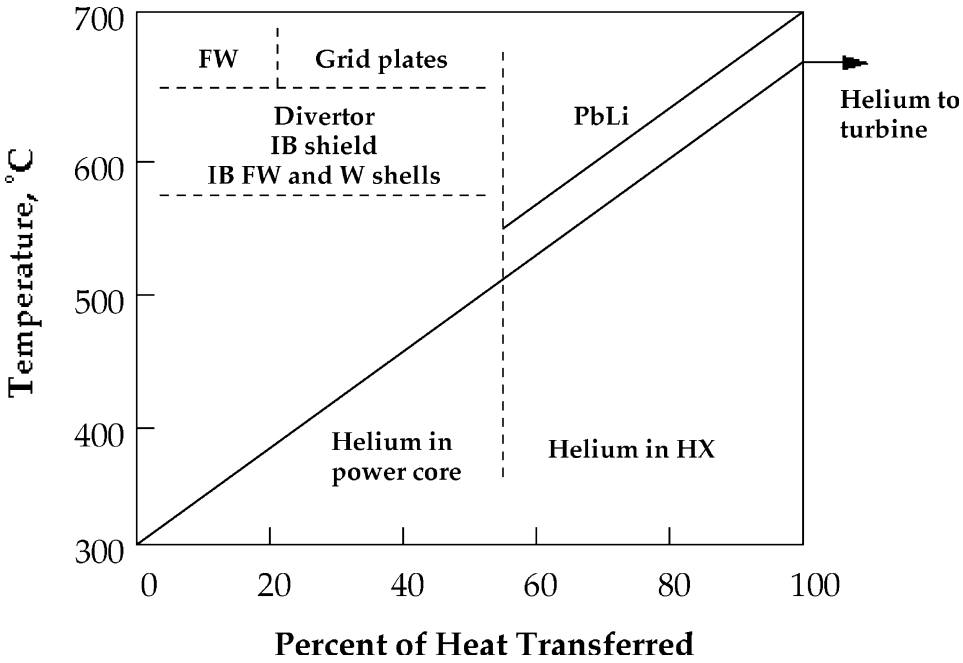

Fig. 16. Temperature–enthalpy diagram for heat exchange between the He coolant and Pb–Li.

where, T_o is the coolant temperature to the turbine, 680 °C; T_s, the sink temperature, 308 °C; r, the compression ratio of the turbine, 3.6; η_x, the recuperator efficiency, 0.96; η_c, the compressor efficiency, 0.92; η_t, the turbine efficiency, 0.92; β, the pressure loss ratio, 1.01; and γ is the heat capacity ratio for He, 1.66.

The power conversion efficiency for the gas cycle with these parameters is 45%. In order to achieve this high value, the efficiencies of each component has to be pushed almost to the limit. Some assumptions are made, such as the design of the recuperator heat exchanger to achieve this efficiency while being able to operate reliably over many years of operation.

Since the efficiency of the power conversion system strongly depends on the temperature and efficiency of each component in the system, it is useful to assess the impact on the power conversion efficiency if the temperature and the efficiencies of each component varies from the design value. Fig. 17 shows the change of the power conversion efficiency due to the change of the parameters in the equation. The change of the efficiency of the recuperator heat exchanger has the largest impact on the efficiency of the power conversion system.

Until the early 1980s, tubular recuperator designs were limited to effectiveness in the range of 81–82%. However, modern recuperators are available with effectiveness of 0.95–0.96 [28]. Some further development is required to achieve the exact set of conditions needed for ARIES-ST, but we believe the extrapolation to our reference value of 0.96 is reasonable.

2.6. Tritium control

For any D–T fusion power plant, tritium control is a difficult issue. For efficient power conversion, the blanket coolant must operate at high temperature. Tritium either will be produced inside the blanket coolant, such as with a self-cooled design, or will permeate into the blanket coolant for a separately-cooled design. This coolant will pass through a heat exchanger to transfer the thermal energy to the power conversion system. To improve the heat transfer rate, the heat exchanger will have a large heat transfer area, with thin-walled tubes maintained at a high

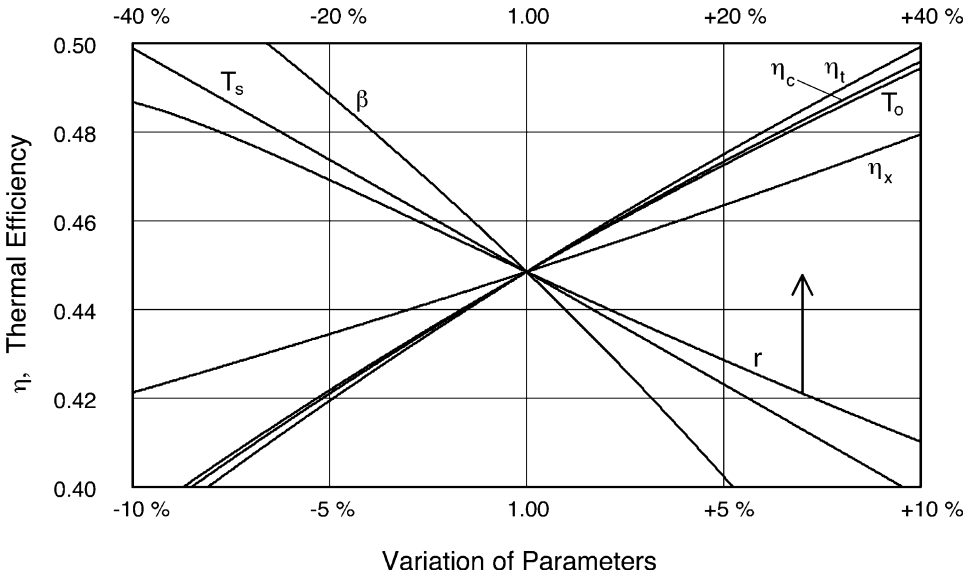

Fig. 17. Variation of thermal conversion efficiency with the key parameters.

temperature. Unfortunately, these are also the conditions for maximum tritium permeation across the wall of the heat exchanger to the environment. The BCSS design set the maximum allowable tritium leakage rate to 10–100 Ci per day [29] although this allowable limit may need to be reduced further.

For ARIES-ST, the problems associated with tritium permeation are even more severe. This is because the coolants are He and Pb–17Li. The tritium solubility in Pb–17Li is very low. Therefore, the tritium partial pressure in Pb–17Li is very high. The tritium partial pressure increase per coolant pass across the blanket has been calculated to be $\sim$0.1 Pa, while the allowable tritium partial pressure across a typical steam generator is $\sim 10^{-5}$ Pa. Therefore, a very efficient tritium recovery system, to be 99.99% efficient, must be designed for tritium recovery from Pb–17Li. A similar efficiency also will be required for tritium recovery from the He stream. Therefore, it is impractical to design a power conversion system with a large heat exchanger exposed to the environment, such as a steam cycle.

A closed-cycle gas turbine was selected in part to alleviate the problems associated with tritium permeation. The flow diagram is shown in Fig. 18. The key element is the recuperator—a large, high temperature heat exchanger. This heat exchanger has a large surface area and operates at high temperature, but is a regenerator heat exchanger. In other words, heat exchange as well as tritium permeation is from a He stream to the same He stream. Therefore, the tritium permeation is internal, and does not exit to the environment. There is another heat exchanger for the waste heat. However, this is a small heat exchanger, operating at 50–100 °C. At this temperature, tritium permeation will not be a severe issue.

The logic is then to design the tritium recovery system to process only a small fraction of the blanket coolants. This will allow the tritium concentration and tritium pressure in the coolants to increase. But since permeation now is not the most critical issue, higher tritium pressure is not as high a concern. In fact, with a higher tritium partial pressure, tritium recovery becomes much easier.

Tritium recovery by permeation is the easiest way to recover tritium, but can be effective only at a moderately high tritium partial pressure. Fig. 19 shows the recent result of tritium recovery from gas by the use of a permeation window. High recovery efficiency has been demonstrated, but

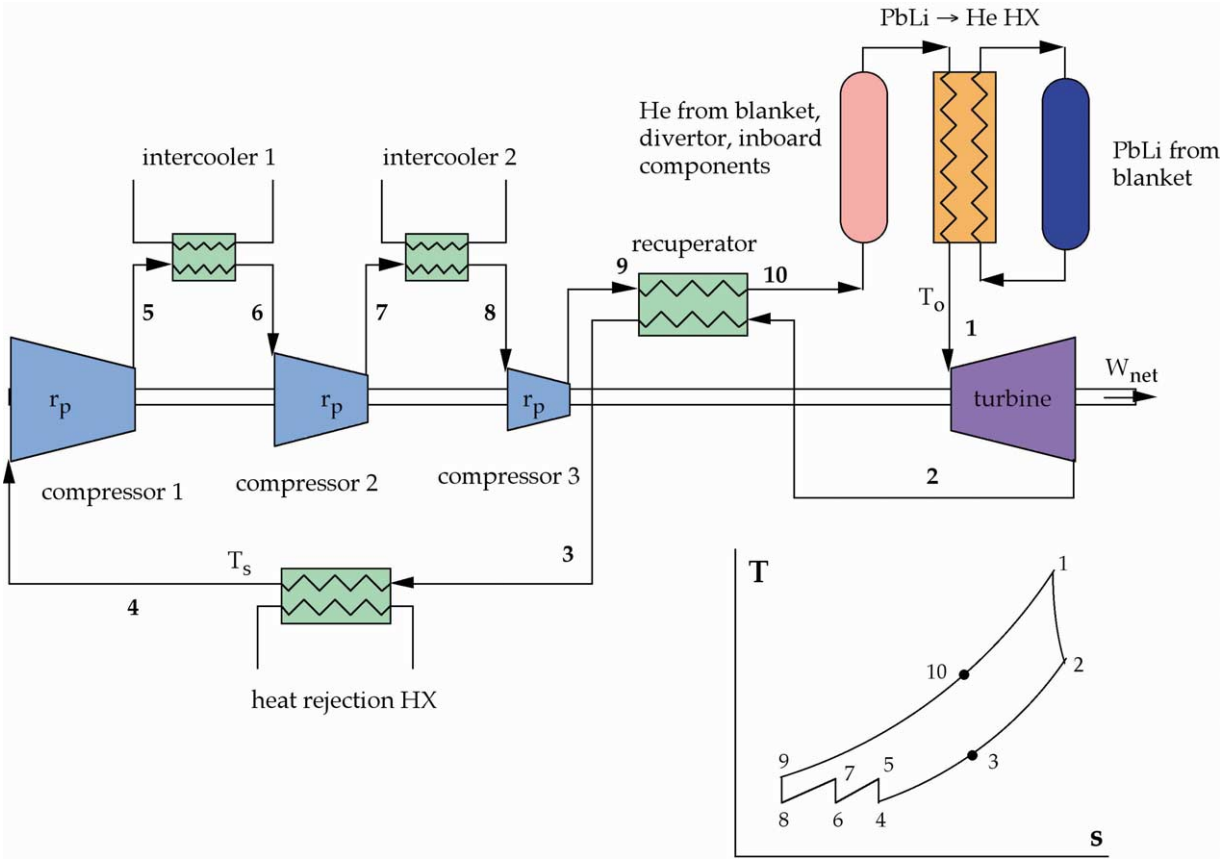

Fig. 18. ARIES-ST three-stage Brayton cycle.

only with a tritium partial pressure higher than ~ 0.1 Pa. The parameters of the tritium system are summarized in Table 8.

The tritium system described here is a high partial tritium pressure, low tritium inventory system. The low tritium inventory is caused by the low tritium solubility in the Pb–Li. The high tritium partial pressure is from the design of the tritium recovery process. With modestly high concentration and the very high tritium partial pressure, the tritium recovery system will not be required to process the entire Pb–17Li and He coolant flows. Only about 0.1% of the He flow and 1% of the Pb–Li coolant flow will have to be processed for tritium recovery. This reduces the size and the required efficiency of the tritium recovery systems. The high tritium partial pressure in the coolants make the use of permeation window for tritium recovery feasible.

As was mentioned above, the reason that a high tritium partial pressure system is acceptable here is that the high temperature, large surface area heat exchanger is a regenerator heat exchanger. The tritium permeated across the wall of this heat exchanger will go only to the same He stream. However, tritium leakage still can be an issue. Since the tritium concentration in the He is 50 Ci per m^3, a tritium He leakage of 0.2 m^3/day will result a tritium loss of 10 Ci per day. One way to resolve this issue is to design a Room Air Detriation System, which will be able to recover the tritium leakage from the coolant loop, as well as from the other power plant system, before it can leak to the environment.

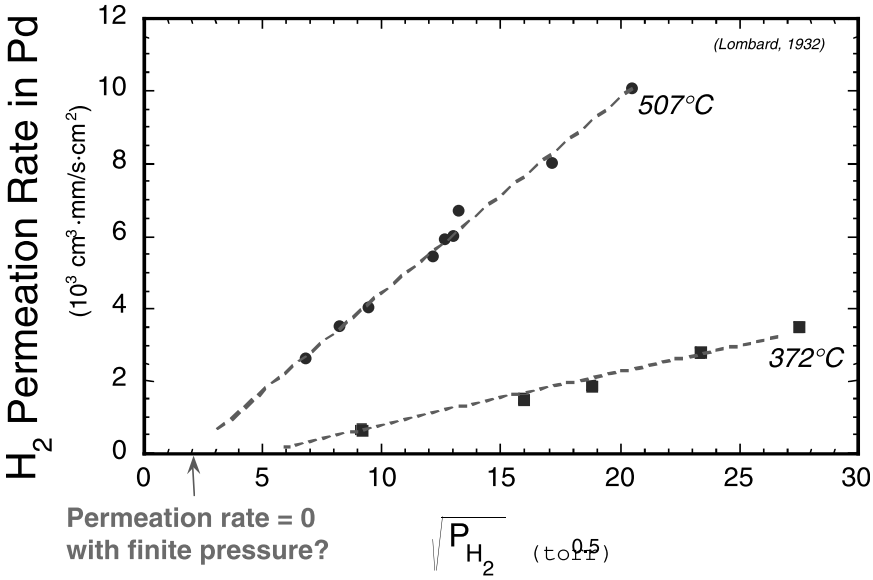

Fig. 19. Tritium recovery from gas by the use of a permeation window.

Table 8
Tritium parameters of ARIES-ST blanket

In Pb–Li	
Pb–Li flow rate	47 450 kg/s
Pb–Li flow rate	2.5×10^5 mol/s
Sievert's constant at 700 °C	2×10^{-8} atom fraction per $Pa^{0.5}$
Tritium source term	1.8×10^{-3} mol/s
Tritium concentration increase per coolant pass	7.2 appb
Tritium concentration in ARIES-ST	0.72 appm
Tritium partial pressure over Pb–Li	7400 Pa
Estimated Pb–Li inventory	150 m^3
Total tritium inventory in Pb–Li	16 g
In He	
He flow rate	1444 kg/s
He density at 500 °C	7.6 kg/m^3
He volumetric flow rate	190 m^3/s
Tritium source term	1.5×10^{-5} mol/s
Tritium pressure increase per coolant pass	0.005 Pa
Tritium pressure in He	5 Pa
Estimated He volume	200 m^3
Tritium inventory in He	1 g

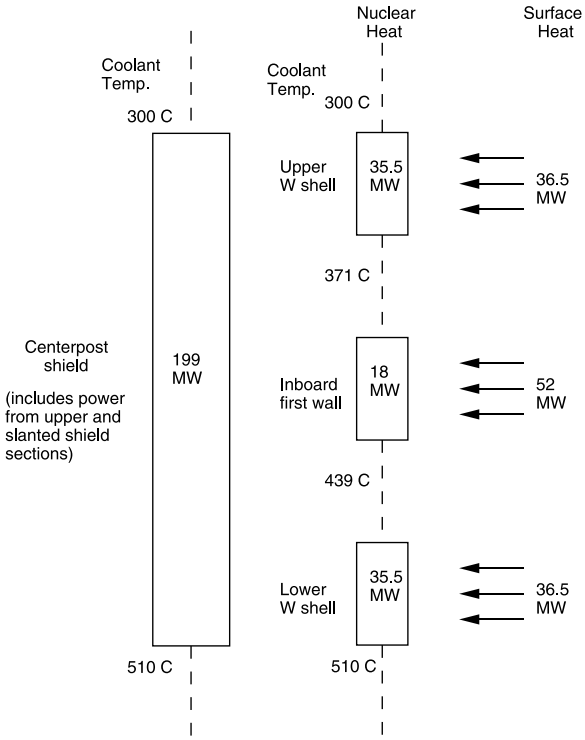

Fig. 20. Diagram showing power distribution on the inboard side of ARIES-ST.

3. Inboard plasma-facing components and shield

As seen in Fig. 1, the inboard side of the ARIES-ST power core consists of inner PF coil shields, the centerpost shield, upper and lower stabilizing shells, and the inboard first wall. All are made of ferritic steel except the stabilizing shells (which are made of tungsten due to the required high electrical conductivity at elevated temperatures), and all are cooled with helium at 12 MPa. Fig. 20 summarizes the inboard power flows. The plasma-facing components (i.e. the first wall and W shells) are grouped into one circuit and the shield sections are grouped into another. The coolant enters on the top at 300 °C and exits on the bottom at 510 °C.

Various coolant configurations were explored in order to optimize the thermal–hydraulics. The inboard space is so limited that once-through coolant paths were determined to be the most effective option. For this cooling geometry, a balance has to be struck between the coolant velocity in the channels, which determines the heat transfer coefficient, and the pressure drop, which determines the pumping power. The pumping power was limited to no more than 10% of the heating power, and the maximum temperature of the ferritic steel structure was limited to $<$ 600 °C.

Particle fluxes to the inboard side of an ST plasma are not well known. In the ARIES-ST design, no armor or coating was applied to the ferritic steel first wall. In principle, the inboard geometry could be tailored to preferentially direct particle fluxes to the tungsten stabilizing shells, which are capable of withstanding both power and particle fluxes far better than ferritic steel. In the design of the W shells, a safety factor of 2 was used to allow for uncertainties in surface heat flux distribution along the inboard wall.

More detailed description of the inboard plasma-facing and shielding components is provided in the following subsections.

3.1. Inboard first wall and tungsten stabilizing shells

The inboard first wall surrounds the inboard shield and is split into two halves, each subtending 180° of circumference. It consists of elliptic coolant channels joined together and oriented with the smaller radius facing the plasma in order to minimize the hoop stresses on the plasma-facing side. Each half of a first-wall assembly has 12 tungsten plates attached to it on each end. The first wall is attached to the inboard shield by joining the two semi-circular first wall assemblies around it (see Fig. 21).

Fig. 22 shows an inner shield segment with a part of the first wall superimposed on it. The channels are welded to each other at the point of contact. A strip of 3 mm thick ferritic steel is welded every five channels, which is then spot welded to a back plate as shown in the figure.

The tungsten shells surround the centerpost at discrete vertical locations. They provide passive vertical stabilization of the plasma, and also act as high-heat flux components covering the transition region between the inboard first wall and the divertors. Tungsten is chosen as the structural material because of its high electrical and thermal conductivity, its high temperature capability, and its resistance to plasma erosion. The effective conductor thickness required for vertical stability is 5 cm. Including the coolant channels, the total thickness is 6.5 cm.

There are 24 plates in each shell, with each plate covering 15° of circumference. The coolant channels are 2.84 cm in diameter spaced at 3.6 cm between center-lines in the cylindrical region of the shell, and increasing to 5.7 cm at the top of the conical region. The cooling channel center-line is 1.76 cm from the front surface of the shell, leaving a thickness of 0.34 cm of W at the front of the channels.

The tungsten plates are joined to the first wall at the top and bottom, making it possible to cool them and the first wall in series. Rather than bonding the two dissimilar metals, flexible manifolds are used to transfer the He gas across the interface (see Fig. 23). An exit manifold from the W plate transfers the gas to an inlet manifold in the first wall. The joining between the W and the ferritic steel occurs across connecting stubs between the manifolds. The stubs are brazed to each other achieving the He gas transfer in a sealed geometry.

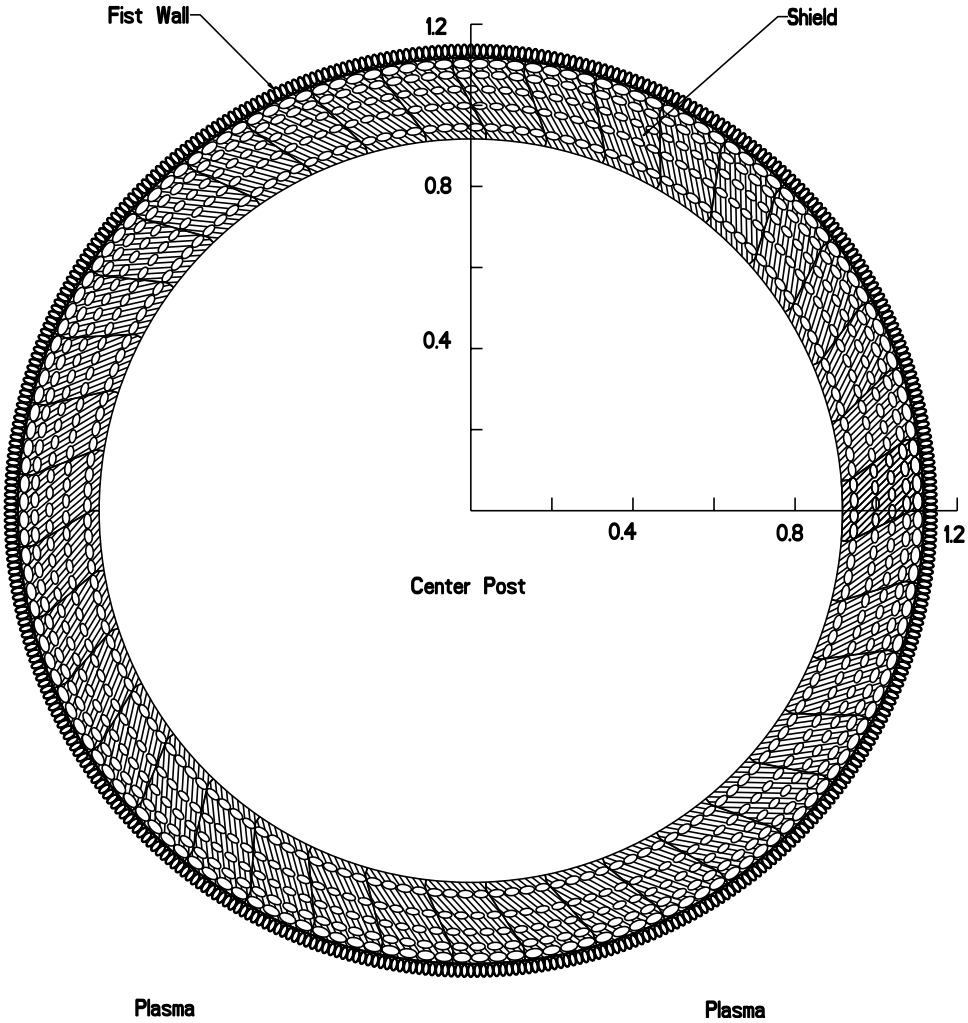

Fig. 21. Mid-plane cross section of the inboard shield.

The velocity in the coolant channels is maintained at 150 m/s. Fig. 24 shows the bulk coolant temperature as it goes from an elevation of +7.7 to −7.7 m. The surface temperatures are also indicated. The surface temperature of the W plates ranges from 668 to 887 °C. This is not much of a concern. The temperature of the first wall peaks from −1.0 to −2.0 m, just below the mid-plane, reaching a peak of 564 °C. At the same point, the average temperature is 530 °C. The pumping power in the coolant system of the plasma facing components is 17.87 MW which is 8.5% of the power recovered. Table 9 summarizes the thermal–hydraulic parameters of the inboard plasma-facing components.

3.2. Centerpost shield

The centerpost shield surrounds the centerpost and protects it from neutron damage and excessive nuclear heating. It serves many additional functions, as summarized in Table 10. It is 20 cm thick and is divided into 39 identical segments; each segment extending the full height of the plasma chamber (a distance of 17 m when each of the divertor shields are included). The nuclear heating

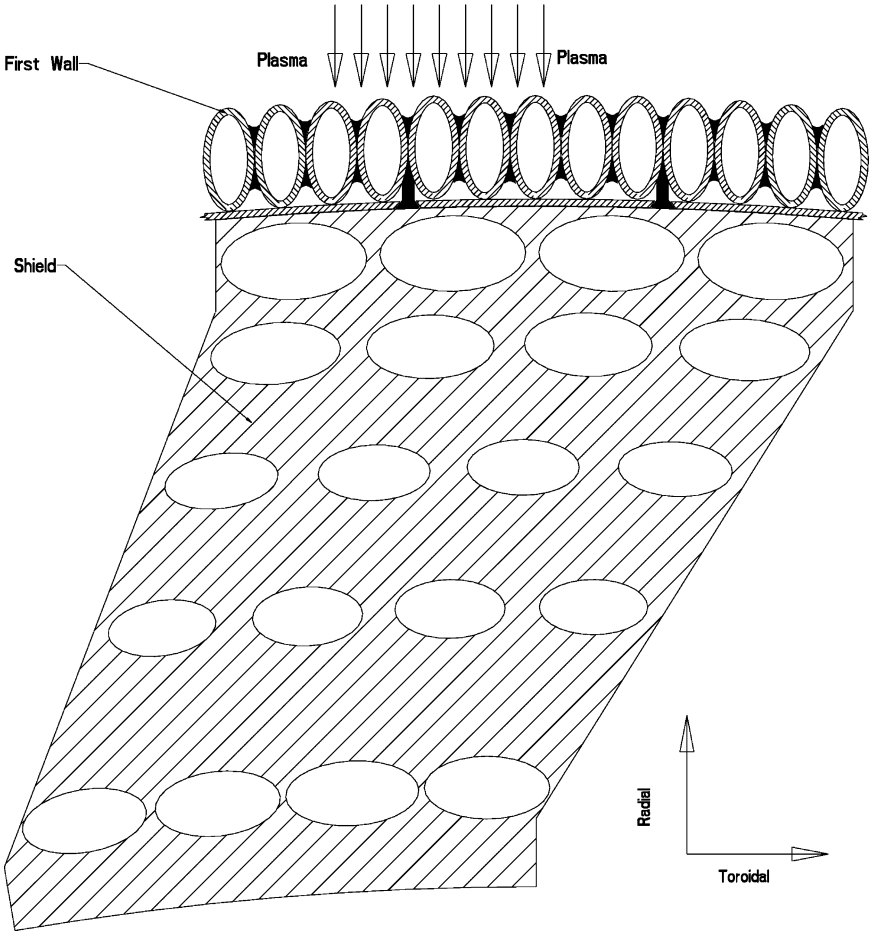

Fig. 22. A segment (1/39th) of inboard shield with superimposed first wall.

in the shield varies by a factor of 2 from the front to the rear. There are five rows of elliptic coolant channels oriented in such a way as to mitigate neutron-streaming.

Besides the cylindrical shield, which extends + 6.5 m, there is a slanted shield of the same thickness extending from +6.5 to +7.7 m and a divertor shield, 10 cm thick extending from +7.7 to +8.5 m. The coolant in the divertor shield passes through the slanted shield and then into the cylindrical shield, proceeding in the same way all the way to the bottom. Both the slanted shield and the cylindrical shield are divided into four zones, each 5 cm thick. The first zone has two rows of coolant channels, and each subsequent zone has one. The shield is divided toroidally into 39 identical segments, a cross section of which is shown in Fig. 22. The dividing lines are slanted to alleviate neutron streaming. When the 39 segments are assembled, they create a cylinder shown in Fig. 21, which is a mid-plane cross section.

Fig. 22 also shows the five rows of elliptic cooling channels distributed in each of the 5 cm shield zones. The shape and distribution of the channels is intended to alleviate neutron streaming. Although the number of coolant channels per row, per segment is the same, the dimensions are varied according to the nuclear heating in each zone.

Fig. 25 shows the specific nuclear heating distribution in the four shield zones as a function of vertical elevation. The nuclear heating peaks at

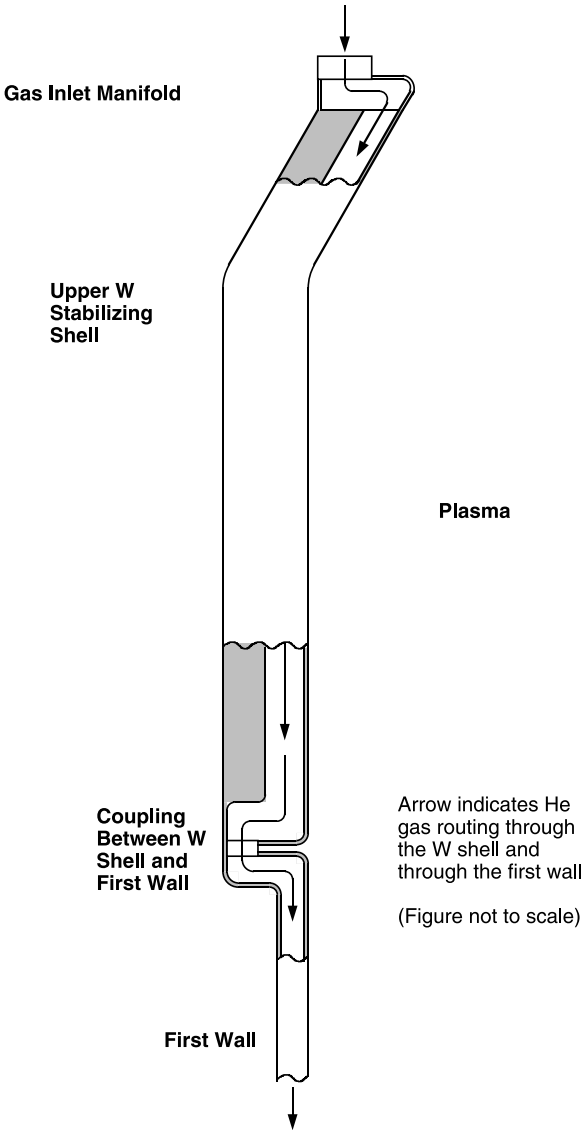

Fig. 23. Tungsten stabilizing shells and their interface with the first wall.

± 1.0 m, reaching a value of 24 MW/m^3. The corresponding heating at the same elevation in the fourth zone is 11.5 MW/m^3.

Ferritic steel has a poor thermal conductivity of 29 W/m K and for this reason, the coolant channel distribution is critical to maintain a shield temperature of <600 °C. Fig. 26 gives the coolant temperature profile in the first shield zone and the front surface temperature of the inboard shield as a function of elevation. The coolant temperature varies from 300 to 510 °C. The peak surface temperature from mid-plane to -5.0 m is 555 °C. At no point in the shield does the temperature exceed 600 °C.

The coolant velocity in all the channels is 105 m/s, and the average coolant fraction in the shield is 13.4%. The pumping power in the shield is 22.9 MW which is 11.3% of the thermal power. Table 11 lists the pertinent thermal–hydraulic parameters of the inboard shield.

4. Divertor

The divertor of ARIES-ST must survive the local environment, including high heat flux, particle flux, and electromagnetic forces. At the same time, it must meet the requirements for an attractive energy source, including low radioactivity, recovery of high-grade heat for energy conversion, maintainability and acceptable cost and reliability. Fortunately, the location of the divertor (far from the plasma center) results in low neutron wall loading (see Fig. 2) and relatively large available space. If a radiative divertor can be established with a deep slot (of the order of 1–2 m long), then the heat fluxes can be maintained quite low on the surrounding structures. Due to the large radiation fraction in the core, only 250 MW of transport power reach the divertors (125 MW each). The average surface heat flux distributed over 128 m^2 of area is only about 2 MW/m^2. The key concerns are the heat flux peaking factor and plasma erosion. Absent more extensive edge physics analysis for an ST power plant, approximate values of peaking factor and particle flux have been extrapolated from ARIES-RS [30].

In the reference design, tungsten was chosen for both the plasma-facing and 'heat sink' material. It exhibits good thermophysical properties, low erosion capability, good high-temperature strength, and has an established and growing database. Its high electrical conductivity made it the logical choice for close-in (plasma-facing) vertical stability shells. One of the concerns with the use of pure tungsten is difficulty with machining and welding. In addition, annealing (which might result from

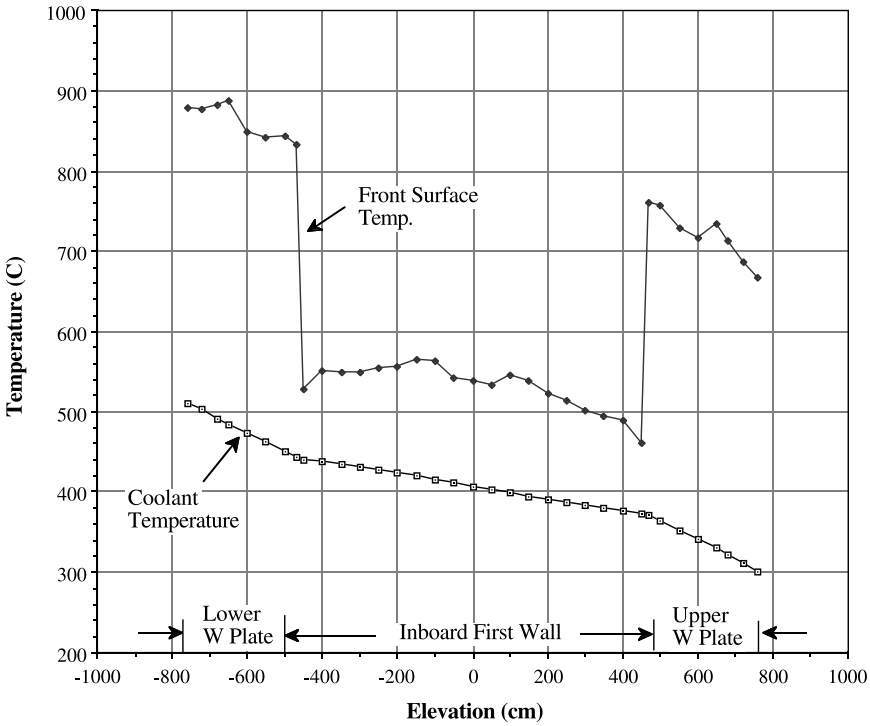

Fig. 24. Coolant temperature profile and peak front surface temperature.

post-heat-treatment bonding) causes very substantial loss in high-temperature yield strength. Therefore, simple design solutions were sought to minimize the need for metal-working. Rhenium addition is known to enhance the ductility and fabricability of tungsten. In this study, an attempt was made to use very simple structures and to maintain the stresses low enough such that pure tungsten could be used, thus reducing the cost.

Helium is the preferred coolant for reasons of safety, materials compatibility, and system integration (since the blanket and other in-vessel systems use He). The primary drawback is its limited heat transfer capability. Therefore, heat

Table 9
Thermal hydraulic parameters of the inboard plasma facing components

	Upper plate	First wall	Lower W plates
Inlet temperature (°C)	300	371.7	438.4
Exit temperature (°C)	371.7	438.4	510
Mass flow rate (kg/s)	193.19	193.19	193.19
Velocity (m/s)	150	150	150
Heat transfer coefficient (W/cm^2 K)	1.37	1.43	1.18
Channel diameter (cm)	2.84	1.81	3.14
Length of channel (m)	2.90	9.0	2.90
Pressure drop (MPa)	0.1304	0.6336	0.0962
Pumping power (MW)	2.5	13.00	2.37

Table 10
Advantages of a 20 cm centerpost shield

Reduces nuclear heat load to centerpost, alleviating centerpost cooling problems and allowing a larger conductor volume fraction
Limits centerpost Joule losses due to neutron-induced transmutations
Allows centerpost to meet Class C requirement for rad-waste while minimizing the rad-waste stream and allowing a replacement interval similar to the first wall/blanket
Reduces radiation damage to Cu conductor
Reduces high thermal gradients in embrittled Cu conductor
Improves power balance by recovering high grade nuclear heat
Reduces radiolysis in the centerpost coolant
Increases blanket TBR, which is marginal

transfer enhancement techniques were explored to ensure acceptable temperatures in the structures [31]. Some of the heat transfer geometries examined include slotted ducts, porous metal flow regions, and normal flow options.

Besides the reference design, free surface designs (in which the coolant is directly exposed to the plasma) were assessed for possible application in ARIES-ST. While free surface divertors offer potential advantages in power handling and lifetime, little R&D has been done such that many fundamental feasibility issues remain. In addition, several factors in ARIES-ST led to healthy design margins: the use of a radiative divertor together with low nuclear heating and ample available space provide for modest heat fluxes and adequate space for He manifolding. For these reasons, the reference design for ARIES-ST uses a solid stationary surface.

4.1. Design description

The divertor region is shown in Fig. 27. On the outboard side, a deep slot is provided to capture 80% of the transport power from the scrape-off layer. On the inboard side, the remaining transport power is distributed along the first wall and tungsten stabilizer plates by tailoring the wall shape with respect to the outermost plasma flux surface.

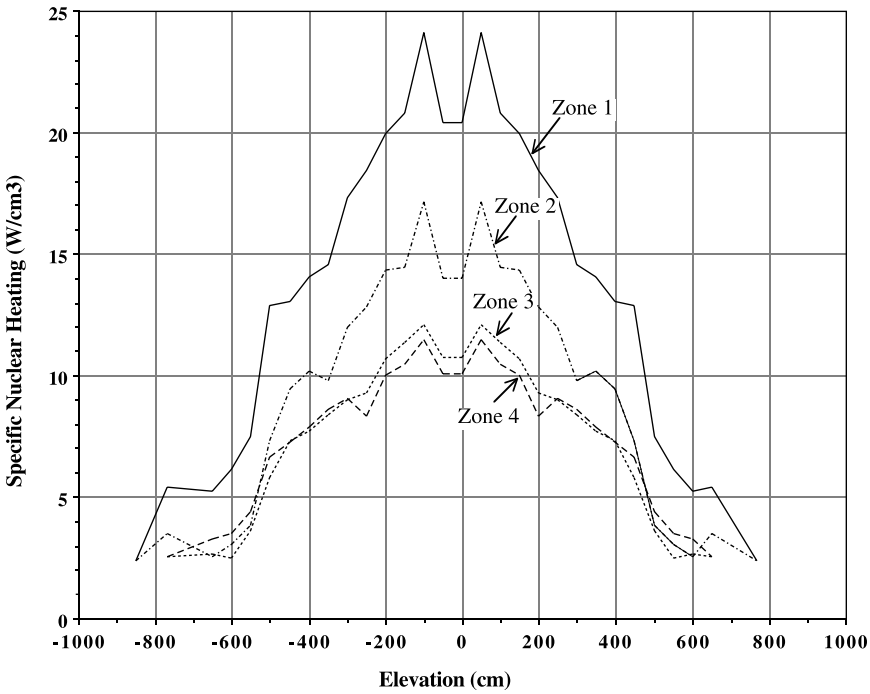

Fig. 25. Specific nuclear heating distribution in the four zones of the inboard shield.

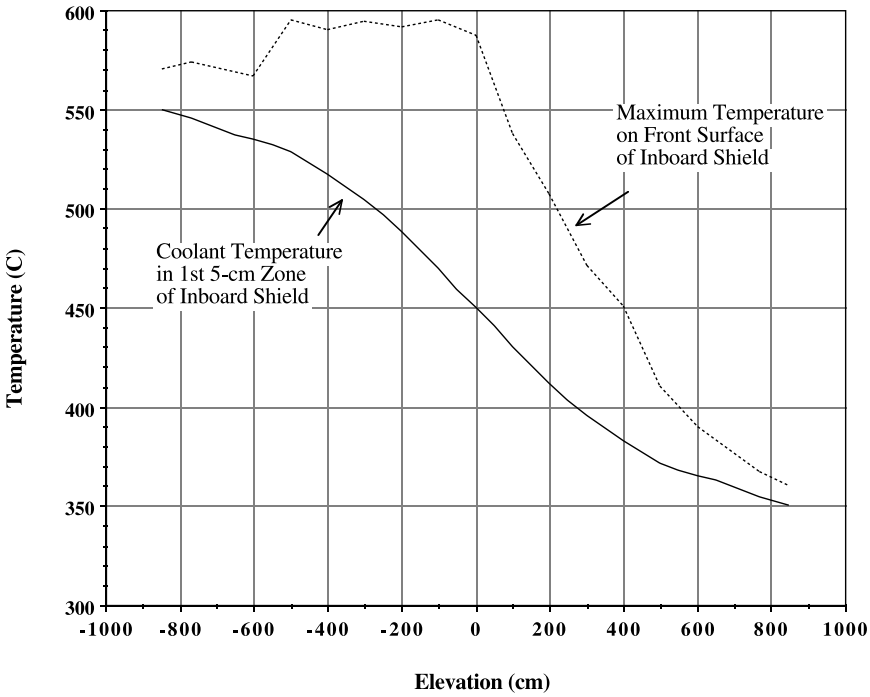

Fig. 26. Coolant temperature profile and peak surface temperature on the front of the inboard shield.

The He coolant is routed to the divertor separately from the other power core components in order to provide the maximum available bulk temperature rise. Toroidal coolant manifolds supply helium to the plasma-facing surfaces. Several internal coolant configurations were considered for surface heat flux removal; in all cases the bulk flow direction is poloidal. The poloidal orientation of the main heat exchange elements allows the pipe bends and joints to be located outside the high heat flux zone and also accommodates uncertainties in the poloidal distribution of heat flux. Further details of the internal cooling geometry are given in the following subsection.

Table 11
Thermal hydraulic parameters of inboard shield

	First zone	Second zone	Third zone	Fourth zone
Power in zone (MW)	79.06	52.12	35.71	35.71
Mass flow rate (kg/s)	72.54	47.82	32.76	32.76
Velocity in channel (m/s)	105	105	105	105
Coolant fraction	19.45%	13.42%	9.64%	10.13%
Equivalent diameter (cm)	2.13	1.72	1.43	1.43
Heat transfer coefficient (W/cm^2 K)	1.11	1.22	1.26	1.26
Inlet temperature (°C)	300	300	300	300
Outlet temperature (°C)	510	510	510	510
Vertical distance (m)	17.0	17.0	15.4	15.4
Pressure drop (MPa)	0.54	0.69	0.78	0.78
Pumping power (MW)	3.96	3.31	2.56	2.56

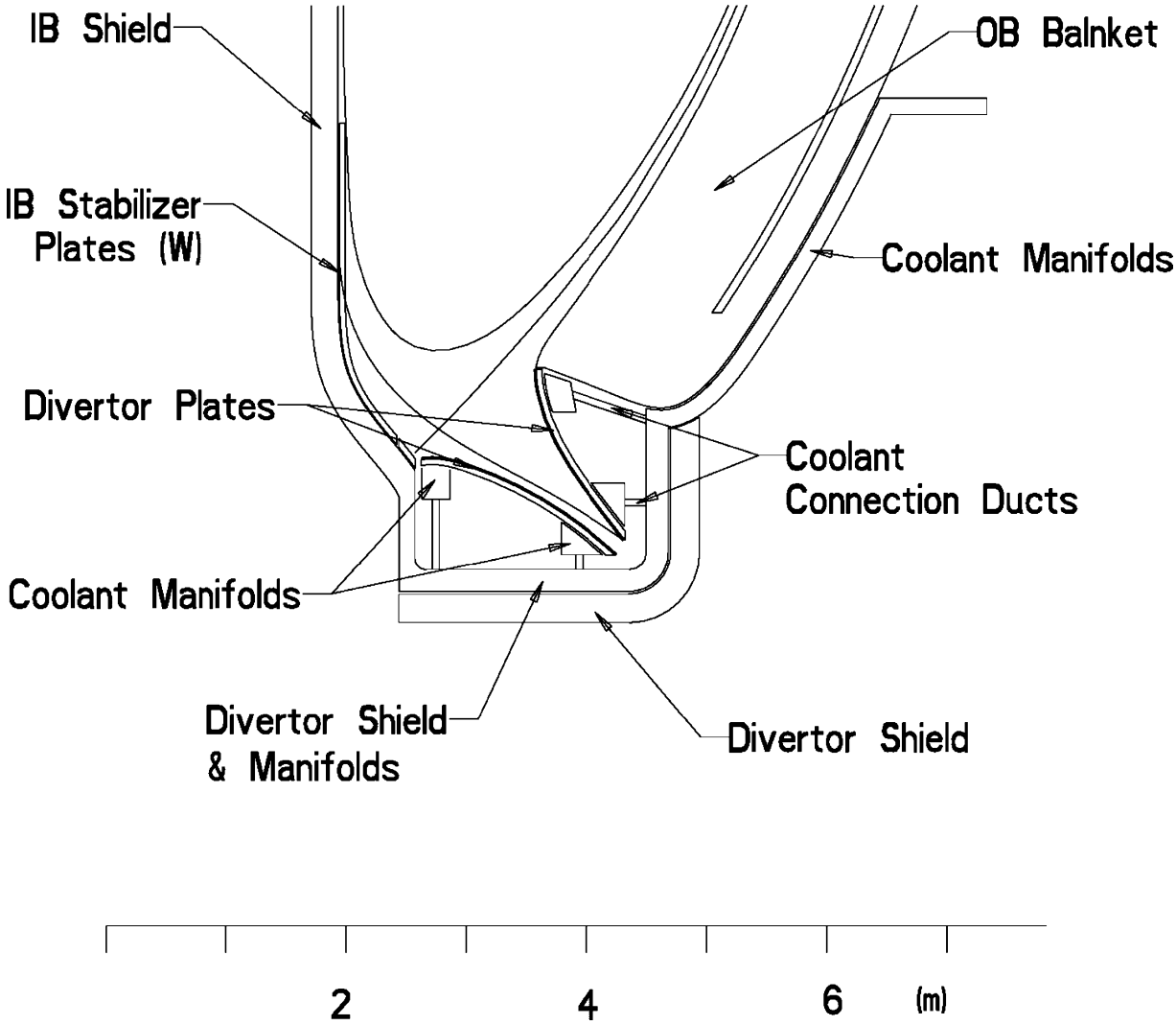

Fig. 27. Elevation view of the divertor region.

4.2. Performance assessment

4.2.1. Thermal–hydraulics

Tungsten has a moderately high thermal conductivity of 100–120 W/m K in the temperature range of interest. Using a conservative value of 100 W/m K, the conduction temperature drop through a 2-mm wall ($\Delta T_s = q\delta/k$) is quite modest: for a surface heat flux $q = 5$ MW/m^2, the temperature rise is only ~ 100 °C. The heat transfer coefficient, h, for helium in ordinary channel flow is given approximately by:

$$Nu = \frac{hd}{k} = 0.018 Re^{0.8}. \tag{7}$$

It depends only very weakly on the channel size ($\propto d^{0.2}$). For a given coolant pressure, the coolant velocity is the dominant parameter. For a He velocity of 100 m/s, we obtain $Nu = 125$ and $h \sim 10^4$ W/m^2 K. The film drop ($\Delta T_f = q/h$) can be quite large in this case: for $q = 5$ MW/m^2, $\Delta T_f = 500$ °C. For a coolant temperature of 500 °C, this would lead to relatively high surface temperature, in excess of 1100 °C. Actually, this is not an

unreasonable temperature for stress-relieved W, which maintains a yield strength of 400 MPa at 1100 °C. However, it is likely to lead to very large temperature gradients in the surrounding structures (leading to high thermal stresses), and also limits the thickness of any additional armor which might be needed to resist plasma erosion. Due to these factors, the primary goal of thermal–hydraulic design was to explore heat transfer enhancement techniques. Three geometries were considered to further enhance the heat removal capability of He: (1) extended surfaces; (2) normal flow; and (3) porous media.

4.2.1.1. Extended surfaces. A 'slotted duct' configuration was considered in conjunction with embedded tungsten rods [32] as an example of an extended surface configuration (see Fig. 28). The slotted duct achieves its heat transfer improvement by increasing the surface area exposed to coolant. If the heat sink material (in this case, W) has a sufficiently high thermal conductivity as compared with the fluid heat transfer coefficient (i.e. $k/ht > 1$), then heat diffuses into the deeper regions of the cooling channel, effectively reducing the local heat flux at the coolant–wall interface. For $k = 100$ W/m K and $h = 10\,000$ W/m^2 K, substantial enhancement can be obtained in this geometry up to 1 cm deep into the channel. The heat transfer 'enhancement factor' is given approximately by [33]:

$$\frac{q}{h\Delta T} = \frac{1}{a+t}\left(a + \sqrt{\frac{2kt}{h}}\right), \tag{8}$$

where a is the channel width and t is the tungsten thickness between channels. In addition to using

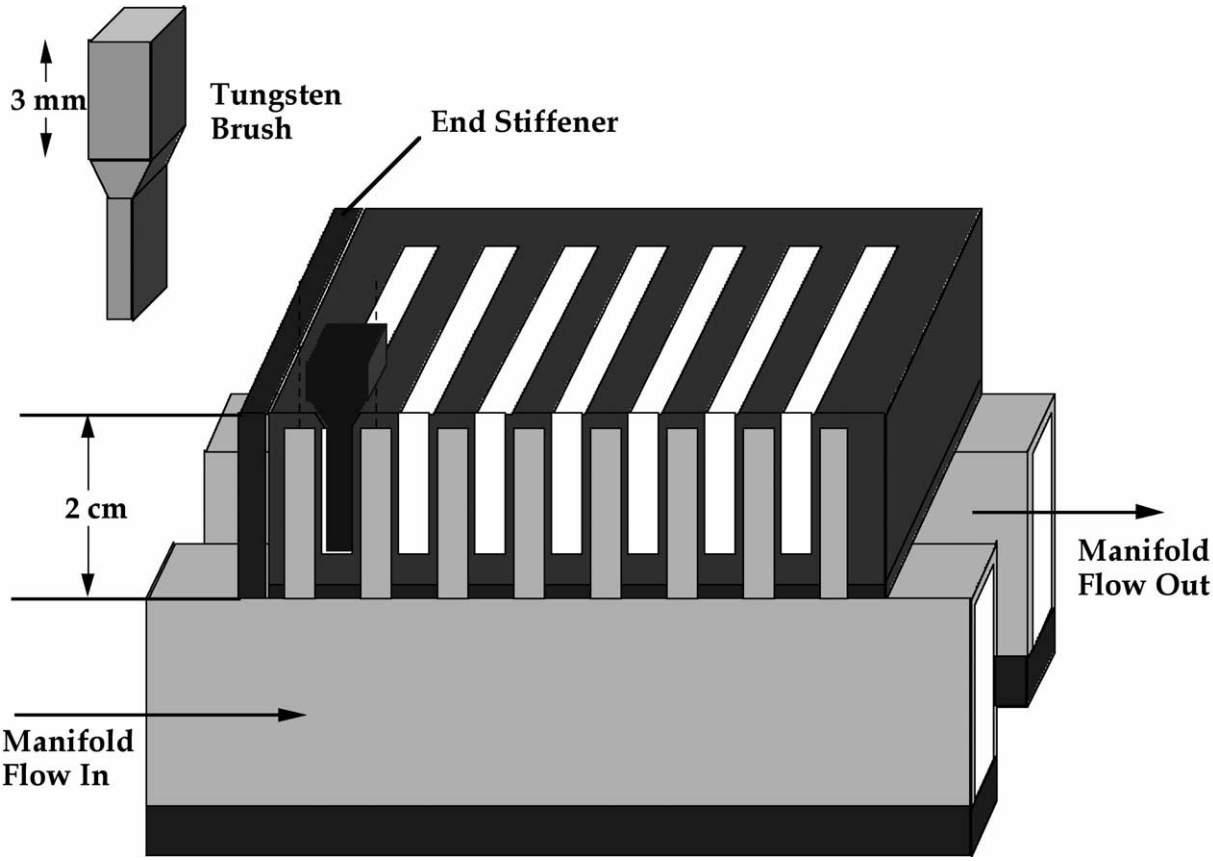

Fig. 28. Configuration of the slotted duct divertor plate.

the 'fin effect', the configuration in Fig. 28 seeks to minimize the coolant path length between the inlet and outlet manifolds. By taking the full temperature rise in a shorter distance, a lower coolant velocity (hence lower pressure drop and pumping power) is possible according to the energy balance equation:

$$\rho C_p v d \Delta T = q'' L, \tag{9}$$

where d is the channel depth.

4.2.1.2. Normal flow. Normal flow configurations also utilize very short coolant path length to enhance heat transfer. In designs such as the 'normal flow heat exchange' [34], the high conductivity of the substrate material acts as an extended surface similar to the slotted duct. In micro-impingement designs [35], high-speed flow of the coolant normal to the heated surface dramatically increases convective heat transfer so that extended surfaces are not needed. These design concepts were not examined in detail, although they appear to be attractive design options.

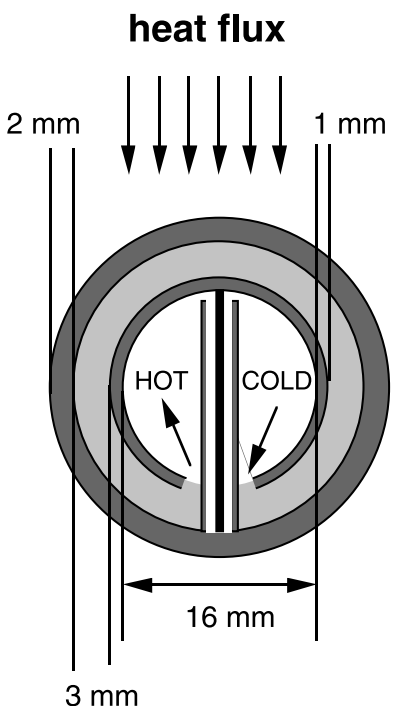

Fig. 29. Porous metal heat exchanger geometry.

4.2.1.3. Porous media. Porous metallic filler materials have been proposed in both sintered bed (PMHX) [36] and foam [37] variants. The reference design concept chosen for ARIES-ST uses a porous metal filler in a cylindrical pipe geometry. This concept was chosen in large part due to simplicity, fabricability and straightforward integration with the manifolding. For the purpose of numerical estimates, the packed bed concept was used because correlations are more readily available.

Fig. 29 shows a tubular design in which the central half-pipes serve as inlet and outlet manifolds and the outer annulus is the primary heat transfer region. Toroidal manifolds supply coolant to the pipes, which are oriented along a poloidal/radial direction. Coolant flows along the axis of the pipes until it is redirected around the circumference. The path length is very short and the effective duct cross sectional area is large, such that low coolant velocity is possible, leading to small pressure drop.

The mass flow rate per channel needed to match the coolant temperature conditions of 300–525 °C while removing an average heat flux of 2 MW/m^2 is 72 g/s, leading to a superficial velocity of 1.88 m/s. The effective heat transfer coefficient, h_{eff}, is given by [36]:

Table 12
Divertor coolant tube parameters

Pipe length	1.5 m
Pebble size, d_p	0.5 mm
Porosity, α	0.4
Power removed per pipe	84 kW
Superficial velocity, V	1.88 m/s
h_p	3159 W/m^2 K
h_{eff}	44 000 W/m^2 K
dp/dx	1.5 MPa/m
Pumping power	846 W

$$h_{\mathrm{eff}} = \alpha h_{\mathrm{p}} + \frac{1}{R_{\mathrm{o}} + [\sqrt{h_{\mathrm{p}} k_{\mathrm{p}} S_{\mathrm{p}}} \tanh(\sqrt{(h_{\mathrm{p}} S_{\mathrm{p}}/k_{\mathrm{p}})} t)]^{-1}}, \quad (10)$$

where S_{p} is the specific surface area; h_{p} is the local particle-to-fluid heat transfer coefficient; R_{o} is the porous medium–wall interface resistance; k_{p} is the porous medium thermal conductivity; and t is the porous medium thickness.

Using the parameters listed in Table 12 and assuming low contact resistance (achieved, for example, by sintering), the effective heat transfer coefficient is 44 000 W/m^2 K. This leads to a film drop of only 114 °C at 5 MW/m^2 local heat flux. The conduction drop through the 2-mm wall is also ~100 °C. Rather large margins can be used to increase the wall thickness for protection against plasma erosion.

The corresponding pressure drop, $\mathrm{d}p/\mathrm{d}x$ and pumping power are found using the Ergun formula: effective heat transfer coefficient, h_{eff}, is given by [36]:

$$\frac{\mathrm{d}p}{\mathrm{d}x} = 150 \frac{1-\alpha^2}{\alpha^3} \frac{\mu_{\mathrm{f}} V}{d_{\mathrm{p}}^2} + 1.75 \frac{1-\alpha}{\alpha^3} \frac{\rho_{\mathrm{f}} V^2}{d_{\mathrm{p}}}. \quad (11)$$

where α denotes the porosity, V is the superficial velocity. The regime is intermediate between laminar and turbulent flow. This design achieves a very modest ratio of pumping power to thermal power removed—only 1%.

4.2.2. Stress analysis

Thermal and stress analysis were performed on both the slotted duct and PMHX options. Parameters for the slotted duct concept are listed in Table 13. Fig. 30 shows the thermal stress results. The boundary conditions are very similar to the first wall; the channels consist of a set of I-beams supported at discrete axial locations by ribs behind the second wall (at the bottom of Fig. 30). Therefore, the structure is free to expand axially but is constrained by symmetry at the mid-plane (at the back side of Fig. 30). Acceptable stresses are possible in this configuration, but concerns over fabrication and reliability led us to adopt the porous metal heat exchanger (PMHX) configuration.

Fig. 31 shows the temperature profile in the outer pipe resulting from a 5 MW/m^2 one-sided heat flux on the PMHX configuration. A 180° U-bend is used to allow relatively unconstrained axial thermal expansion. As a result, peak stresses occur at the location of attachment, rather than at the location of peak temperature.

Fig. 32 shows the attachment of the heat exchanger pipes to the manifolding. As shown in Fig. 33, the peak stresses occur at the location of attachment, rather than at the location of peak temperature. These results were obtained by constraining the axial location of the attachment but allowing rotation. Fully-constrained displacements at the attachment led to unacceptable stresses; therefore, careful design of these interconnects is essential.

5. Materials issues

ARIES-ST incorporates several materials for which data and design criteria are required. The required level of detail depends on the functional importance of the component and the status of the database. Materials of particular interest include: ODS and precipitation-hardened (PH) copper

Table 13
Slotted duct parameters for 100 m/s coolant velocity

	Case I 1 × 10 mm	Case II 2 × 10 mm	Case III 3 × 10 mm
Re	22 000	40 400	56 000
Δp (MPa)	0.39	0.18	0.12
Pumping power [a]	1.3%	1.2%	1.2%
ΔT_{b}	1014	507	338

[a] As a fraction of the total thermal power.

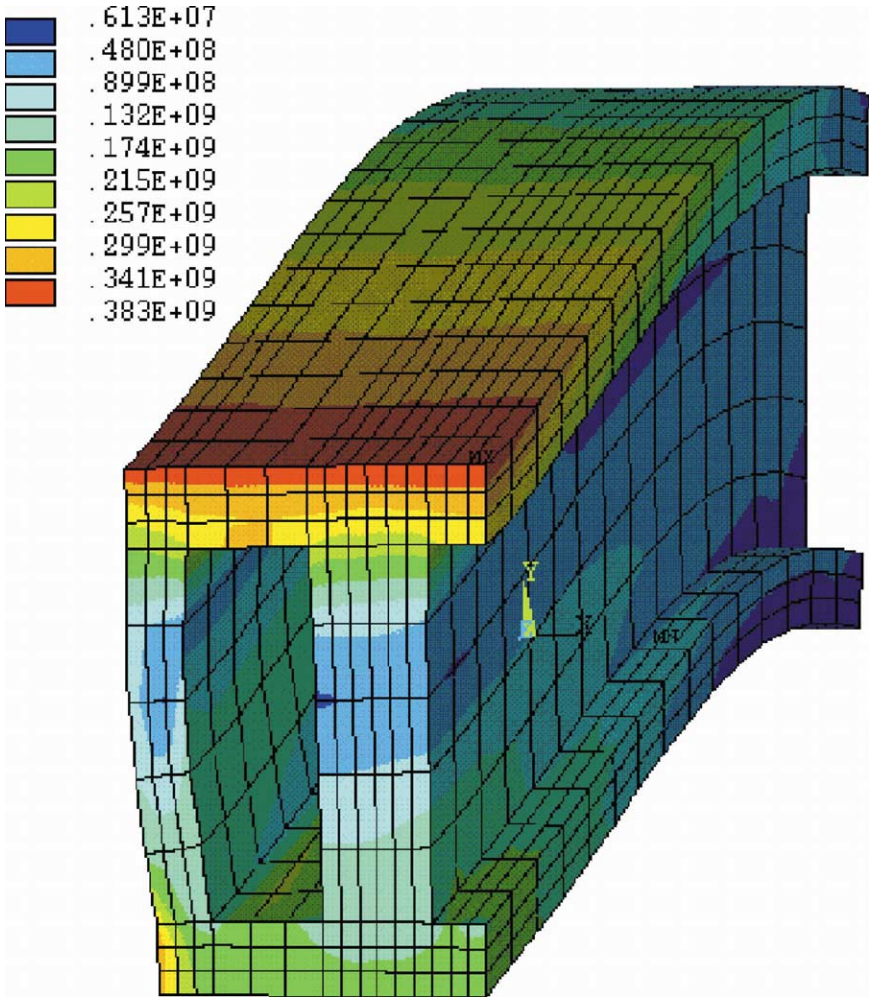

Fig. 30. Thermal stresses in the slotted duct divertor plate.

alloys for the center post, aluminum alloys for the TF outer shell (which also serves as the vacuum vessel), low-activation ferritic steel alloys (with and without oxide-dispersion strengthening) for the first-wall and blanket structural and piping material, low-thermal-conductivity SiC or SiC/SiC composites for the thermal insulation between the ferritic steel and the hot Pb–Li breeder, and tungsten for the stability shell and divertor coolant tubes (which also serve as plasma-interactive components).

The key data needs include thermophysical and mechanical properties of individual materials, fabrication and joining techniques, hydrogen isotope behavior, and compatibility between solid materials and coolant–breeder fluids. For each data need, the materials input includes both the present status of the database and projections of progress that can be reasonably achieved over the next 25–50 years. Performance limits based on existing data together with reasonable projections of possible advances allow optimization of system performance based on credible extrapolations.

Key sources of data and design criteria include the ITER Material Properties Handbook (IMPH) [38] and the ITER Interim Structural Design Criteria (IISDC) [39]. The status of on-going research efforts in the US and international

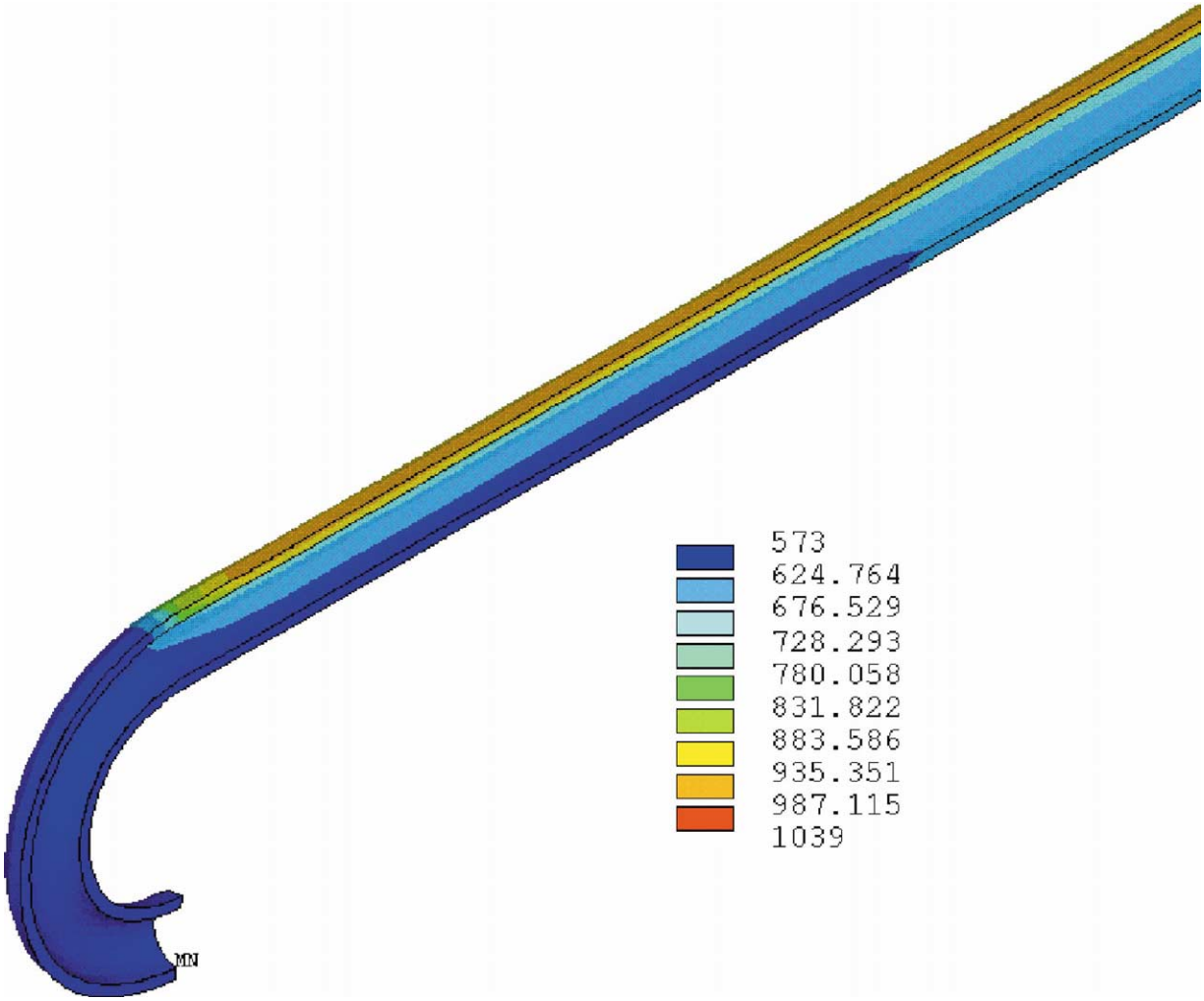

Fig. 31. Temperature profile in the divertor outer pipe.

programs are obtained from Semiannual progress reports of the US fusion materials program, summaries of IEA meetings and proceedings of materials conferences (e.g. ICFRM).

This section focuses on first-wall, blanket and divertor materials issues. The issues for the center post and the outer-shell and vacuum vessel materials are described elsewhere [4].

5.1. Ferritic steel first wall and blanket structure

High temperature, high-strength, low-activation, ferritic steel alloys with ODS are considered as a relatively near-term option for the structural material of the blanket. The first wall is a He-cooled box-like structure constructed of low-activation ferritic steel. In the early designs, the He entered the first wall at 350 °C and exited to the blanket at a temperature low enough to keep the ferritic steel first-wall maximum temperature $\leq$ 500 °C. Higher ferritic steel temperatures ($\leq$ 500 °C) were allowed in the blanket region. For thermodynamic efficiency reasons, the design was later modified to have the He enter at 300 °C and exit to the blanket at 420 °C, while allowing the peak ferritic steel temperature to be $\leq$600 °C.

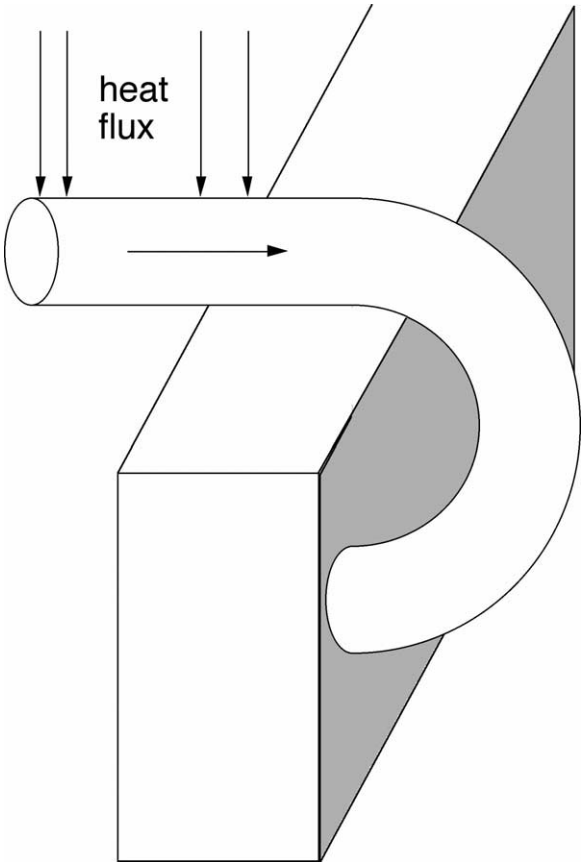

Fig. 32. Attachment of divertor tubes to manifolding.

Considerable effort has been directed toward establishing design criteria for ferritic steels (which are not included in the current IMPH). Fabrication specifications and design limits are contained in both the US ASME Boiler & Pressure Vessel Code [40] and the French RCC-MR [41] for modified 9Cr–1Mo (Fe–9Cr–1MoVNb). As the RCC-MR Code has developed design guidelines for these steels up to higher temperature (600 °C) than the ASME Code, it is used here as a reference. The major alloying constituents of the code-qualified ferritic steel are: Fe–(8–9)wt.%Cr–(0.85–1.05)wt.%Mo–(0.18–0.25)wt.%V–(0.06–0.10)wt.%Nb.

Fig. 34 shows the RCC-MR minimum ultimate tensile strength (UTS), minimum yield strength (YS) and design stress intensity factor (S_m) for this ferritic steel, along with the creep-limited design stress intensity (S_{mt}) for a 3-year design life. The tensile and thermal creep data for the Japanese F-82H and the IEA heat F-82H(mod) were compared with the data RCC-MR code-qualified modified 9Cr–1Mo. Even with the irradiation-induced softening of ultimate tensile and yield strengths of the F82-H above ≈ 400 °C, the tensile properties of F82-H remained within the scatter band of those for Fe–9Cr–1MoVNb. Also, the minimum thermal creep strength properties of modified 9Cr–1Mo provide a reasonable lower bound for those of F-82H and F-82H(mod). Thus, the established design-limit stresses and criteria for the code-qualified modified 9Cr–1Mo can be used as a reasonable lower bound for the new low activation steels [42].

The short-term tensile properties resulted in a design stress intensity limit of 148 MPa at 500 °C, 128 MPa at 550 °C and 103 MPa at 600 °C. However, thermal creep for 3 full-power-years of operation limited these stresses to 110 MPa at 550 °C and 61 MPa at 600 °C. The design stress intensity directly limits the average (through-wall) primary stress and indirectly (though multiplicative factors) the primary bending and secondary thermal stresses.

Since the low thermal creep strength of traditional and low-activation ferritic steels in the temperature range of 550–600 °C, the decision was made to use an oxide-dispersion-strengthened (ODS) ferritic steel. These alloys were developed as part of the Fast Breeder Reactor programs in the US and Japan. The strengthening of these alloys comes from the dispersion of fine particles of Y–Ti–O. Although not optimized for fusion reactor applications, the compositions (in wt.%) of the alloys currently being tested as low-activation ODS ferritic steels are in the range of Fe–(11–14)Cr–(2–3)W–(0.4–0.5)Ti–(0.2–0.7)Y2O3, with some extra oxygen (≈ 0.1 wt.%) added. Given the limited database for such low-activation ODS ferritic steels, the tensile and creep properties of F82-H were shifted (upward) by only 50 °C (for $T > 400$ °C). Recent data reported by of Mukhopadhyay et al. [16] suggest that such a shift is reasonably conservative, from a design perspec-

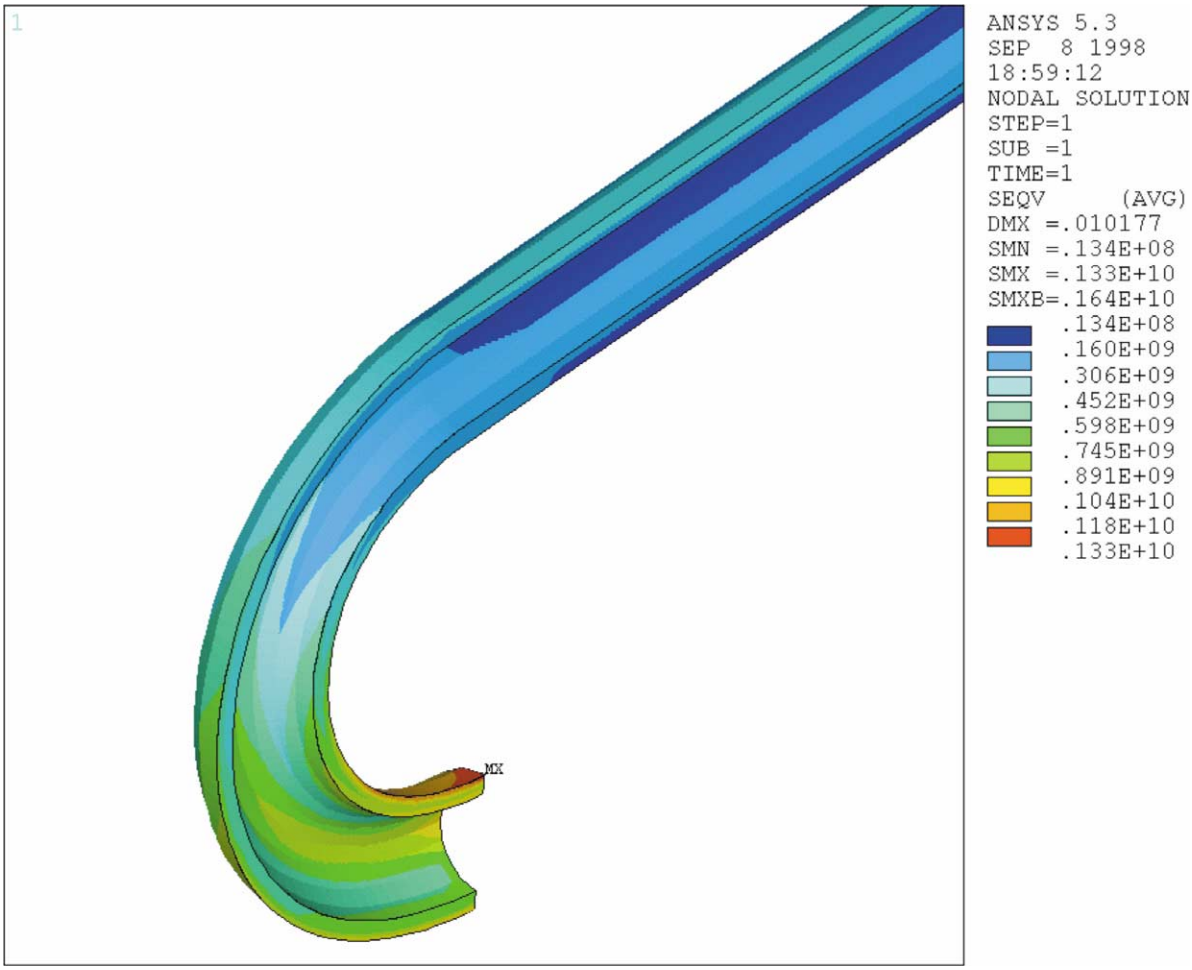

Fig. 33. Thermal plus pressure (12 MPa) stresses in the divertor outer pipe.

tive, for the thermal creep properties of ODS ferritic steel. The assumed UTS, YS, S_m and thermal-creep-limited (3-year lifetime) S_{mt} for ODS ferritic steel are shown in Fig. 35.

The design changes in coolant inlet temperature (from 350 to 300 °C) and in the structural material (ferritic steel to ODS-ferritic steel) have introduced additional uncertainties into the design because of the uncertainties in the databases for both ferritic steel and ODS-ferritic steel. The simultaneous effects of neutron damage and He transmutation on the DBTT of ferritic steel are not well established. While a minimum ferritic steel temperature of 300 °C may be reasonable based on neutron irradiations without significant He production, some question remains regarding the effects of He on the DBTT of ferritic steels such as F82-H. With regard to the switch to ODS-ferritic steel, the uncertainties in the database increase significantly. Also, special joining techniques are required for ODS-ferritic steel in order to retain the creep-resistance of these alloys. Advances in stir-friction welding (which does not require melting of the alloy for joining) look promising as a solution to the joining process. However, questions remain regarding the lower temperature limit

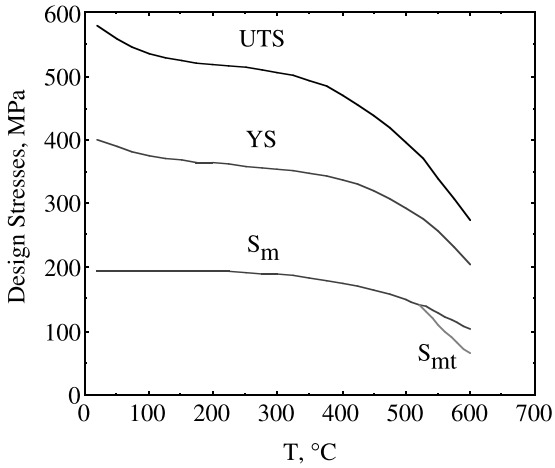

Fig. 34. RCC-MR design stresses for modified 9Cr–1Mo. (Fe–9Cr–1MoVNb): UTS is the minimum ultimate tensile strength, YS is the minimum yield strength, S_m is the time-independent design stress intensity, and S_{mt} is the time-dependent stress intensity based on thermal creep limits for a 3-year design life.

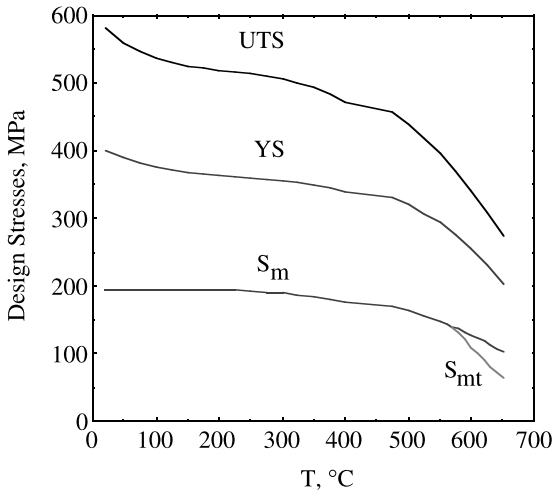

Fig. 35. Assumed design stresses for ODS ferritic steel: UTS is the minimum ultimate tensile strength, YS is the minimum yield strength, S_m is the time-independent design stress intensity, and S_{mt} is the time-dependent stress intensity based on thermal creep limits for a 3-year design life. These results were derived from the RCC-MR design stresses for modified 9Cr–1Mo by assuming a 50 °C shift in properties for $T > 400$ °C.

(based on DBTT) and the upper temperature limit (based on possible irradiation-induced softening) of ODS ferritic steels. More data are needed in these areas, along with further optimization of ODS ferritic steels for fusion applications.

5.2. SiC flow channel inserts

In the ARIES-ST blanket, a thermal and electrical barrier is required between the hot, flowing Pb–17Li breeder and the ferritic steel structural material. The Pb–17Li enters the blanket zone at 480 °C and exits the blanket zone at 700 °C, carrying a substantial fraction of the total heat and the tritium generated. With the maximum structural temperature of the steel set at 600 °C, the thermal barrier must sustain a maximum $\Delta T \approx 100$ °C and be compatible with the Pb–17Li up to 700 °C. SiC has been proposed as the thermal barrier. Fabrication and performance issues which have been raised regarding the SiC insulating layer are: finding a viable and economic fabrication method for up to 10-mm thickness, achieving a thermal conductivity ≤ 4 W/m K and an electrical resistive ≥ 0.1–1.0 Ω cm. compatibility with flowing Pb–17Li, tritium inventory in the SiC layer, and radiation-stability in the presence of neutron displacement damage, He production and H production.

The thermomechanical requirements for ARIES-ST SiC are modest, such that the existing database is generally adequate. In fact, one of the key issues for SiC/SiC in first wall applications—namely low thermal conductivity is a desired property in the ARIES-ST blanket. The thermal conductivities of both the α and β phases of SiC are sensitive to the levels of porosity and impurities. Values reported about 25 years ago for lower purity β-SiC are 25.5 W/m K at 200 °C and 15.5 W/m K at 1000 °C [43]. Neutron irradiation causes a significant reduction in thermal conductivity, particularly for irradiation temperatures $\leq$ 700 °C. By taking advantage of the reduction in thermal conductivity of SiC with impurities, as well as the further reduction due to irradiation, thermal conductivities ≤ 4 W/m K appear to be achievable. However, the introduction of impu-

rities to lower thermal conductivity is constrained by Pb–Li-breeder compatibility considerations.

The focus of the following discussion is on the hydrogen isotope behavior (diffusion, solubility and permeation in and through SiC) and compatibility with PbLi (see Section 5.3 for compatibility). As most of the reliable hydrogen-isotope data are for β-SiC, the results and discussion are restricted to the performance and properties of β-SiC.

As the SiC in ARIES-ST is not a plasma-facing material and tritium is not a transmutation product for SiC, the hydrogen isotope source terms for the SiC would be direct recoil from the Pb–17Li arid adsorption/diffusion/solubility of gas phase tritium from the Pb–17Li. The amount of direct-recoil tritium, as well as He, from the Pb–17Li is predicted to be very small because of the presence of the Pb.

Reliable tritium diffusivity data are available for β-SiC in the temperature range of 1100–1500 °C [44,45]. Even at 1100 °C, diffusion is so slow that it would take >10 years for tritium to penetrate the 10 mm of SiC. Extrapolating to lower temperatures implies that the kinetics of tritium transport in β-SiC are so slow that tritium retention may be a non-issue. Tritium/deuterium solubility data are available for the temperature range of 1000–1600 °C for the same thin samples (50–90 μm) as were used in the diffusivity experiments. Since the difficulty of achieving thermodynamic equilibrium within 8 h exposure to 1–100 kPa of deuterium and the difficulty of distinguishing surface concentrations from bulk concentrations, the solubility data are directly applicable only for the temperature range of 1500–1600 °C. Considerable analysis and data reduction were required to extend the solubility database down to 1000 °C. With the corrections for surface concentrations and non-uniform bulk distribution of tritium, the solubility of deuterium in the bulk was found to vary with the square-root of the deuterium pressure. At 1000 °C, the solubility is calculated to be only 0.14 appm(Si)/$Pa^{0.5}$, where appm(Si) are hydrogen-isotope atoms per million Si atoms. As the solubility of hydrogen isotopes increases with decreasing temperature for β-SiC, the extrapolation down to 700 °C gives an equilibrium concentration of ≈ 0.8 appm(Si)/$Pa^{0.5}$. However, the result is not meaningful for ARIES-ST design analysis as it would take an extremely long time to achieve this equilibrium concentration.

5.3. Compatibility of SiC and ferritic steel with liquid Pb–17Li

Hubberstey and Sample summarize the data on the stability of oxide, nitride and carbide ceramics in Li and Pb–Li [46]. They report that β-SiC has been observed to be stable in 800 °C Pb–17Li for 1500 h based on the information presented in [47]. Hubberstey and Sample [46] also performed thermodynamic equilibrium calculations which showed that, in general, carbide and nitride ceramics are more stable than oxide ceramics in liquid Li-based liquid metals and that, the stability increases as the Li level decreases. In particular, their calculations support the observation that β-SiC is stable in Pb–17Li. However, based on further consultation with one of authors of [47], it was learned that the experiment was conducted in static Pb–17Li, that the SiC samples were not characterized (in terms of porosity, impurities, etc.) prior to testing, and that the samples degenerated after 4500 h of exposure at 800 °C [48]. Thus, while thermodynamic equilibrium calculations suggest that SiC should be stable in Pb–17Li, there are no data on well-characterized SiC or SiC/SiC composites to support these calculations.

The database for Pb–Li/ferritic steel compatibility is reasonably well established in the temperature range of 400–550 °C for times up to approximately 1 year [49]. Most of the data are for the traditional ferritic steels, rather than the low-activation steels. These steels experience a homogeneous dissolution in Pb–17Li without the formation of a superficial corrosion layer. The high solubilities of Fe, Cr and Ni (Ni is not contained in the low activation steels) in Pb–17Li result in material loss rates that increase with time linearly and with velocity (V) raised to the 0.875 power. The velocity dependence suggests that the rate-controlling mechanism for mass loss rate is the diffusion of Fe, Cr and Ni in the Pb–17Li. According to [49], the mass loss rate (v in μm/

year) can be expressed as:

$$v = 8 \times 10^9 \exp\left[-\frac{25\,690}{1.98T}\right] V^{0.875} d^{-0.125} \quad (12)$$

where T is temperature in K, V is velocity in m/s, and d is the hydraulic diameter in m.

Other studies have been performed to determine the effects of an aluminum oxide layer on the ferritic steel [50] and of magnetic fields [51] on the material loss rate. An aluminum oxide layer on MANET-I ferritic steel was successful in suppressing material loss for approximately 1 year at 450 °C in Pb–17Li flowing at 0.3 m/s. The magnetic field appears to increase the material loss rate by ≈30%, although scatter in the data is large and it is not clear that velocities are accurately calculated in the very slow-flowing Pb–17Li for the non-magnetic and magnetic field cases.

For the ARIES-ST design, the Pb–17Li between the SiC thermal barrier and the ferritic steel structure is 3.5-mm thick and 200-mm long, giving a hydraulic diameter of ~7 mm. The Pb–17Li is essentially stagnant in this region except for small thermal convection effects. For the purposes of upper-bound design estimates, let us assume that the flow rate to be used in Eq. (12) is 0.001 m/s and $d = 0.007$ m. This would give material loss rates (for a 3-year lifetime) of only 2 μm at 450 °C, 5 μm at 500 °C. 15 μm at 550 °C and 37 μm at 600 °C. Using the experimental results directly from [51] for slow-flowing (thermal-convection driven at ≈0.03 m/s) Pb–17Li loops in a magnetic field would give <50 μm of material loss rate at 460 °C for a 3-year lifetime. Thus, as long as the Pb–17Li is quasi-stagnant between the SiC and the ferritic steel, material loss rate does not appear to be a problem for the ARIES-ST design.

5.4. Tungsten

Tungsten was chosen as the stabilization shell and divertor material. The divertor consists of porous metal heat exchanger tubes described in Section 4. While the fabrication of these tubes is a challenge, the focus of this section is on the material properties of the final product. The decision to use unalloyed W rather than more-easily-fabricated W–Re alloys was based on reducing material costs. This issue will have to be revisited after a final fabrication cost estimate is made for the unalloyed W. The W pipes will be formed by powder-metallurgy hot-isostatic-pressing, cold-worked, and stress-relieved to give optimum tensile strength and ductility. Tungsten is generally stress-relieved (as opposed to recrystallized annealed) at ≈1150 °C. Stress-relieved tungsten has significantly higher ultimate-tensile (≈680 vs. ≈300 MPa at 800 °C) and yield (≈600 vs. ≈125 MPa at 800 °C) strength than annealed tungsten in the ARIES-ST operating temperature range (250–800 °C with He as the coolant). The main structural issues with the stress-relieved W are related to ductility and fracture toughness both before and after irradiation. The nominal DBTT for stress-relieved W is given as 100–200 °C. However, tensile properties show very low ductility (uniform elongation, total elongation, and reduction-in-area) in the range of RT-500 °C. In general, there are few data points in this range and there is considerable scatter in the data for cold-worked/stress-relieved W depending on impurities, amount of cold-work, and time-temperature of the stress relief. Whatever the DBTT of unirradiated W, the DBTT is expected to increase with neutron irradiation. It is possible that the whole divertor will eventually be in the 'brittle' regime with regard to design rules. Thus, the fracture toughness and/or the critical stress intensity become extremely important design parameters. With the database for the fracture toughness of unirradiated W relatively limited, one can only expect that the database for irradiated W is even more limited. Thus, there remains a materials issue with regard to the performance of the W divertor.

Recently, Japanese colleagues have demonstrated some success, on a small laboratory scale, in decreasing the DBTT of W and increasing the re crystallization temperature by the dispersion of nano-size particles of TiC (0.2–0.5 wt.%) in the fine-grained W [52]. However, their data are based on impact three-point-bend tests (with no notch), as compared with the traditional notched Charpy test used to determine DBTT. Nonetheless, they

achieved significant improvement in absorbed energy, as compared with pure W, for temperatures in the range of 125–275 °C. Plans are in progress to irradiate such samples in HFIR to see if the improvement in low-temperature ductility withstands irradiation damage.

An additional design feature, which may require optimization and demonstration, is the joining of the W divertor to the ferritic steel He manifolds in the back of the divertor. Brazing has been specified with Ti–25Cr–3Be as a possible braze material.

6. R&D needs

In the design of the ARIES-ST power core, extrapolation from existing technologies was allowed in order to provide an attractive end-product, but minimized in order to obtain a credible design with an acceptable development program. Cases in which extrapolations beyond established technology were necessary are identified below as key R&D needs. The ordering is not intended to imply relative importance.

As is often the case, uncertainties in materials performance, especially when subjected to the complete fusion environment, give rise to several key issues. This arises due to the use of novel or untested materials, or to the particular environmental conditions to which they are subjected.

1) Radiation damage effects and lifetime of advanced ferritic steel. Ferritic/Martensitic steel has been a top candidate alloy in fusion programs around the world for years. Its database is large and growing. Nevertheless, radiation damage and lifetime remain important issues.
2) Temperature limits of ferritic steel. Low-activation ferritic steels are usually limited in operating temperature to less than 550 °C. In order to enable efficient power conversion, a higher temperature limit is needed. In combination with the novel use of heat from PbLi, a maximum steel temperature of 600 °C would allow a Brayton cycle with $>45\%$ conversion efficiency.
3) Fabricability and radiation damage in tungsten. The excellent thermophysical and plasma-interactive properties of tungsten helps to provide a credible solution to divertor design. However, pure tungsten suffers from low fracture toughness and uncertain irradiation damage characteristics.
4) Electrical resistance of SiC. Measured resisivities for SiC/SiC composite often are not available. MHD analysis of the French TAURO concept used a value of 0.2 Ω cm, which had been measured for solid SiC at 1000 °C [12]. Their finding was that the MHD pressure drop in a duct with such a resisivity is tolerable. For comparison, the resisivity of ferritic steel at 500 °C is 95×10^{-6} Ω cm and for Pb–17Li 130×10^{-6} Ω cm. Pure alumina would have a resisivity of 10^6 Ω cm at 1000 °C.
5) Lifetime of SiG under irradiation. Little is known about the radiation damage limit of SiC. Besides defect and interstitial accumulation, significant composition changes are possible due to (n, α) reactions in both C and Si. A maximum 'burnup' of 3% has been assumed in this study. The fact that the requirements on mechanical properties of SiC in ARIES-ST are modest makes this issue less critical.

   Compatibility between materials at high temperature raises several concerns both inside the blanket and in the heat transport loop. The primary concern results from the use of PbLi, for which very limited data are available.
6) Compatibility of Pb–17Li with ferritic steel. All of the steel structure in the blanket segment and the steel wall of the liquid metal coolant tubes are thermally insulated from the flowing Pb–17Li by a SiC liner. However, there is a gap of stagnant Pb–17Li between the steel wall and the flowing Pb–17Li for pressure equalization. At this Pb–17Li/steel interface the temperature will be slightly higher than the local helium temperature (525 °C). For self-cooled Pb–17Li blankets with a flow velocity of up to 2 m/s and ferritic steel as structural material, a

maximum allowable interface temperature of 470 °C has been used previously, based on a corrosion rate of less than 20 μm/year. It is assumed that a limit about 50 °C higher can be allowed in the stagnant gap. Further testing is needed to demonstrate acceptable mass transport and corrosion levels.

7) Compatibility of Pb–17Li with SiC. The maximum interface temperature between the two materials is below 700 °C. Tests at ISPRA have shown that the two materials are compatible at 800 °C under stagnant conditions [12]. Tests in flowing Pb–17Li are under way, and are hoped to establish acceptable performance.

8) High temperature heat exchanger compatibility with Pb–17Li. The main penalty for raising PbLi to 700 °C is the need to develop a high-temperature PbLi heat exchanger. This was considered a reasonable trade-off, although the technology needs to be demonstrated. The top candidate heat exchanger material is SiC. Due to the absence of radiation damage concerns, relatively higher thermal conductivity composites should be possible.

9) Liquid metal MHD effects. In the dual coolant design, MHD effects are eliminated in regions of high heat flux (first wall and divertor) by using He as the coolant. In the breeder zone, the MHD pressure drop is expected to be reduced as compared with conducting wall designs due to the use of insulating inserts. However, detailed MHD analysis was not performed to estimate 3-D entrance and manifolding effects, which could substantially affect the flow patterns and total pressure drop. Besides incurring locally large pressure drops, hot spots in the breeder could result if the flow is affected by MHD interactions. Better multi-dimensional modeling tools are needed in order to examine complex geometric effects accurately.

10) Tritium containment. Tritium containment is always an issue for DT fusion, but especially for high temperature systems with low solubility coolant (PbLi). In ARIES-ST, the primary He coolant is used directly in the turbine and power conversion components. At the same time, maximum allowable leakage rates from the plant are low (10 Ci/day) and heading lower. Careful design of the power conversion, tritium extraction and tritium containment systems is needed.

11) Ferromagnetism. Ferritic steel is ferromagnetic. This raises new classes of issues that have not been adequately addressed in R&D programs. The issues generally fall into three categories: (a) Plasma interactions, (b) Engineering interactions, and (c) Diagnostic interactions

Plasma interactions include concerns over field ripple, impacts on start-up, and general position and shape control. Engineering interactions include forces during normal operation, disruption forces, and MHD effects on liquid metal flows. Diagnostic interactions include interference with magnetic field measurements.

12) Edge physics. In self-cooled systems, surface heat flux usually is a more dominant concern than volumetric neutron heating. Surface heat flux concerns are exacerbated in ARIES-ST due to the long inboard coolant, path length and uncertain inboard power flows. Divertor cooling is always a major concern. Both peak and average values of surface heat flux dominate many aspects of engineering design; yet large uncertainties exist due to the lack of adequate data and models for ST edge physics. Hopefully, operation and analysis of ST experiments around the world will help to better define the edge conditions.

7. Summary and conclusions

We have described a fusion power core design that is compatible with a spherical torus (ST) containing a highly-elongated, low aspect-ratio power plant plasma. Although the plasma beta for the optimized design is high, the fusion power density is comparable with previous studies such as ARIES-RS [1,2].

The first wall and blanket were selected based on evolution of existing knowledge. The first wall materials and design have enjoyed extensive R&D in international programs and have been shown to meet the requirements of the expected ARIES-ST environment. Probably the most daring extrapolation in blanket technology is the use of very high temperature PbLi breeder/coolant contained in SiC channel inserts. Modest additional R&D could be performed to validate assumptions regarding materials compatibility and liquid metal MHD behavior. The benefits of this approach are substantial; higher thermal conversion efficiency has a direct impact on the bottom-line cost of electricity by reducing not only the power core size, but also the entire plant size.

Design of the plasma-facing components for ARIES-ST was challenging, due in large part to uncertainties in the edge physics. A divertor design very similar to ARIES-RS was chosen to meet the requirements of a highly radiative divertor plasma [1,2]. As a consequence of the ST configuration, there is insufficient space for a full inboard divertor slot. Fortuitously, inboard transport power flows are expected to be substantially reduced as the aspect ratio decreases, such that the net heat flux is not unreasonable. As ST plasma may 'bump up' against the inboard first wall, the inboard vertical stability shells are designed as plasma-facing components in the transition region between the inboard steel wall and the divertor. Finally, the very long path length for inboard cooling poses special challenges for cooling of the inboard components.

We believe the ARIES-ST power core is a credible design concept with a firm footing in established technologies. Reasonable extrapolations enable us to meet all of the design requirements while achieving a high power conversion efficiency and acceptable capital cost.

References

[1] ARIES Team, F. Najmabadi, Overview of the ARIES-RS reversed-shear tokamak power plant study, Fusion Eng. Des. 38 (1997) 3–25.

[2] ARIES Team, M.S. Tillack, S. Malang, L. Waganer, X.R. Wang, D.K. Sze, L. El-Guebaly, C.P.C. Wong, J.A. Crowell, T.K. Mau, L. Bromberg, Configuration and engineering design of the ARIES-RS tokamak power plant, Fusion Eng. Des. 38 (1997) 87–113.

[3] F. Najmabadi, the ARIES Team, Spherical torus concept at power plants: The ARIES-ST study, Fusion Eng. Des. this issue.

[4] W. Reiersen, F. Dahlgren, H.-M. Fan, C. Neumeyer, I. Zatz and the ARIES Team., The toroidal field coil design for ARIES-ST, Fusion Eng. Des. this issue.

[5] L. Bromberg, S. Pourrahimi, J.H Schulz, P.Titus, S. Jardin, C. Kessel, W. Reiersen and the ARIES Team, Superconducting poloidal field magnet engineeering for the ARIES-ST, Fusion Eng. Des. this issue.

[6] L. El-Guebaly, I. Sviatoslavsky and the ARIES Team, ARIES-ST nuclear analysis and shield design, Fusion Eng. Des. this issue.

[7] H.Y.Khater, E.A. Mogahed, D.K. Sze, M.S. Tillack, X.R. Wang and the ARIES Team, ARIES-ST safety design and analysis, Fusion Eng. Des. this issue.

[8] S. Jardin, C.E Kessel, J. Menard, T.K Mau, R. Miller, F. Najmamabadi, V.Chan, L.Lao, Y.R. Linliu, R.L. Miller, T.Petrie, P. Politzer, A.D. Turnbull and the ARIES Team., Physics basis for spherical torus power plants, Fusion Eng. Des. this issue.

[9] L.M. Waganer, F. Najmabadi, M.S. Tillack, What must demo do, Proceedings of IEEE 16th Symposium on Fusion Engineering, Champaign, IL (October, 1995) IEEE No. 95CH35852, IEEE, Piscataway, NJ, 1995.

[10] G.R. Tynan, J. Liberati, P. Pribyl, R.J. Taylor, B. Wells, Externally-driven H-mode studies in CCT, Plasma Phys. Control. Fusion s-638 (1996) 1301–1305.

[11] S. Malang, M.S. Tillack (Ed.), Development of Self-Cooled Liquid Metal Breeder Blankets, Forschungszentrum Karlsruhe Report FZKA 5581, 1995.

[12] L. Giancarli, et al., Design requirements for SiC/SiC composites structural material in fusion power reactor blankets, Fusion Eng. Des. 41 (1998) 165–171.

[13] A.S. Perez Ramirez, A. Caso, L. Giancarli, N. Le Bars, G. Chaumat, J.F. Salavy, J. Szczepanski, TAURO: a ceramic composite structural material self-cooled Pb–17Li breeder blanket concept, J. Nucl. Mater. 233–237 (1996) 1257–1261.

[14] M.S. Tillack, S. Malang, High-performance PbLi blanket, Proceedings of IEEE 17th Symposium on Fusion Engineering, San Diego, CA (October 1997) IEEE No. 97CB36131, IEEE, Piscataway, NJ, 1997.

[15] M. Rieth, Irradiation Project Manitu 300 °C, Rev. 30 August 1996.

[16] D.K. Mukhopadhyay, F.H. Froes, D.G. Gellis, Development of oxide dispersion strengthened ferritic steels for fusion, J. Nucl. Mater. 258–263 (1998) 1209–1215.

[17] T. Kuwabara, H. Kurishita, S. Ukai, M. Narui, S. Mizuta, Y. Yamazaki, H. Kayano, Superior Charpy impact properties of ODS ferritic steel irradiated in JOYO, J. Nucl. Mater. 258–263 (1998) 1236.

[18] S. Ukai, T. Nishida, T. Okuda, T. Yoshitake, R&D of oxide dispersion strengthened ferritic martensitic steels for FBR, J. Nucl. Mater. 258–263 (1998) 1745.
[19] J. Saito, T. Suda, S. Yamashita, S. Ohnuki, H. Takahashi, N. Akasaka, T. Nishida, S. Ukai, Void formation and microstructural development in oxide dispersion strengthened ferritic steels during electron-irradiation, J. Nucl. Mater. 258–263 (1998) 1264.
[20] P. Norajitra, Thermohydraulics Design and Thermomechanics Analysis of Two European Breeder Blanket Concepts for DEMO, Forschungszentrum Karlsruhe Report FZKA 5580, June 1995.
[21] W.M. Kays, M.E. Crawford, Convective Heat and Mass Transfer, third ed, McGraw-Hill, 1993.
[22] W.M. Rohsenow, J.P. Hartnett, E.N. Ganic, Handbook of Heat Transfer Applications, second ed, McGraw-Hill, 1985.
[23] ANSYS Version 5.3, Swanson Analysis Systems, Houston, PA.
[24] ASME Boiler and Pressure Vessel Code, Section III, Code Case N-47-29, 1995.
[25] F.A. Garner, R.J. Puigh, Irradiation creep and swelling of the fusion heats of PCA, HT9 and 9Cr–1Mo irradiated to high neutron fluence, J. Nucl. Mater. 179–181 (1991) 577–580.
[26] M.B. Toloczko, F.A. Garner, C.R. Eihozer, Irradiation creep and swelling of the US fusion heats of HT9 and 9Cr–1Mo to 208 dPa at ~ 400 °C, J. Nucl. Mater. 212–215 (1994) 604–607.
[27] S. Malang, H. Schnauder, M.S. Tillack, Combination of a self-cooled liquid metal breeder blanket with a gas turbine power conversion system, Fusion Eng. Des. 39–40 (1998) 561.
[28] R. Schleicher, A.R. Raffray, C.P. Wong, An assessment of the Brayton cycle for high performance power plant, Proceedings of 14th ANS Topical Meeting on Technology of Fusion Energy, Park City, UT, 15–19 October 2000, Fusion Technol. 39 (2001) 823–827.
[29] D.L. Smith, G.D. Morgan, M.A. Abdou, et al., Blanket Comparison and Selection Study Final Report, Argonne National Laboratory Report ANL/FPP-84-1, 1984.
[30] C.P.C. Wong, E. Chin, T.W. Petrie, E.E. Reis, M.S. Tillack, X. Wang, I. Sviatoslavsky, S. Malang, D.K. Sze, and The ARIES Team, ARIES-RS divertor system selection and analysis, Fusion Eng. Des. 38 (1997) 115–137.
[31] D.L. Youchison, M.G. Izenson, C.B. Baxi, J.H. Rosenfeld, High heat flux testing of helium-cooled heat exchangers for fusion applications, Fusion Technol. 29 (1996) 559–570.
[32] R.E. Nygren, D.L. Youchison, R.D. Watson, High heat flux tests on heat sinks armored with tungsten rods, Proceedings of Fifth International Symposium on Fusion Nuclear Technology (ISFNT-5), Rome, Italy (September 1999), Fusion Eng. Des. 49–50 (2000) 303–308.
[33] M.S. Tillack, M.A. Abdou, Z. Gorbis, T. Takeda, F. Tehranian, A.Y. Ying, Helium-cooled divertor for ITER: a study of cooling options, requirements and limits, University of California Los Angels Report UCLA-ENG-93–22, April 1993.
[34] M.G. Izenson, J.A. Valenzuela, Normal flow heat exchanger for divertor panel cooling, Fusion Technol. 21 (1992) 1828.
[35] G.O. Campbell et al., Metal Microchannel Coolers for High Heat Flux Applications, SAE 951442, presented at the SAE Aerospace Atlantic Conference, Dayton OH, 22–25 May 1995.
[36] J.H. Rosenfeld, J.E. Toth, A.L. Phillips, Emerging applications for porous media heat exchangers, Proceedings of International Conference on Porous Media and Their Applications in Science, Expo Industry, Kona, HA, 16–21 June 1996.
[37] A.J. Sherman, B.E. Williams, M.J. DelaRosa, R. LaFerla, Characterization of porous cellular materials fabricated by CVD, Proceedings of 1990 MRS Fall Meeting, Boston, MA, 26–30 November 1990.
[38] J.W. Davis (Ed.), TIER Material Properties Handbook, ITER Doc. S74-RE-1-97-08-01 W1.5, August 1997.
[39] S. Majumdar (Ed.), ITER Interim Structural Design Criteria, ITER Doc. S74-RE-2-97-07-30 W1.2, July 1997.
[40] Materials, Part A—Ferrous Materials Specifications, ASME Boiler and Pressure Vessel Code (ASME B&PVC), Section II, pp. 599–603 and Part D-Properties, pp. 292–294, 432–433 and 492–495, July 1995.
[41] RCC-MR, Régies de Conception et de Construction des Matériels Mechaniques des ílots Nucléaraires RNR, Tomes I et II, AFCEN, édition 1987.
[42] J. Wareing, A.A. Tavassoli, Assessment of martensitic steels for advanced fusion reactors, Trans. 13th International Conference Structural Mechanics in Reactor Technology (SMiRT-13), Port Alegre, Brazil, vol. 1, Div. E: pp. 563–574, ISBN 85-7025349-4, 13–18 August 1995.
[43] R.C. Marshall, J.W. Faust, C.E. Ryan (Eds.), Silicon Carbide-1973, Proceedings on Third International Conference on Silicon Carbide, Miami Beach, 17–20 September 1973, pp. 668–673.
[44] R.A. Causey, W.R. Wampler, J.R. Retelle, J.L. Kaae, Tritium migration in vapor-deposited -silicon carbide, J. Nucl. Mater. 203 (1993) 196–205.
[45] R.A. Causey, W.R. Wampler, The use of silicon carbide as a tritium permeation barrier, J. Nucl. Mater. 220–222 (1995) 823–826.
[46] P. Hubberstey, T. Sample, Thermodynamics of the interactions between liquid breeders and ceramic coating materials, J. Nucl. Mater. 248 (1997) 140–146.
[47] V. Coen, H. Kolbe, L. Orecchia, M. Delia Rossa, High Temperature Corrosion of Technical Ceramics, Elsevier Applied Science, Amsterdam, 1989.
[48] V. Coen, Personal Communication, 1998.
[49] T. Flament, P. Tortorelli, V. Coen, H. Borgstedt, Compatibility of materials in fusion first wall and blanket structures cooled by liquid metals, J. Nucl. Mater. 191–194 (1992) 132–138.

[50] H.U. Borgstedt, H. Glasbrenner, Z. Peric, Corrosion of insulating layers on MANET steel in flowing Pb–Li, J. Nucl. Mater. 212–215 (1994) 1501–1503.
[51] A. Terlain, T. Dufrenoy, Influence of a magnetic field on the corrosion of austenitic and martensitic steels by semi-stagnant Pb17Li, J. Nucl. Mater. 212–215 (1994) 1504–1508.
[52] Y. Kitsunai, H. Kurishita, H. Kayano, Y. Hiraoka, T. Igarashi, T. Takida, Microstructure and impact properties of ultra-fine grained tungsten alloys dispersed with TiC, J. Nucl. Mater. 271–271 (1999) 423–428.